

Fourier reconstruction for diffraction tomography of an object rotated into arbitrary orientations

Clemens Kirisits¹
clemens.kirisits@univie.ac.at

Michael Quellmalz²
quellmalz@math.tu-berlin.de

Monika Ritsch-Marte³
monika.ritsch-marte@i-med.ac.at

Otmar Scherzer^{1,4}
otmar.scherzer@univie.ac.at

Eric Setterqvist⁴
eric.setterqvist@ricam.oeaw.ac.at

Gabriele Steidl²
steidl@math.tu-berlin.de

April 19, 2021

¹Faculty of Mathematics
University of Vienna
Oskar-Morgenstern-Platz 1
A-1090 Vienna, Austria

²Institute of Mathematics
Technical University Berlin
Straße des 17. Juni 136
D-10623 Berlin, Germany

³Institute of Biomedical Physics
Medical University of Innsbruck
Müllerstraße 44
A-6020 Innsbruck, Austria

⁴Johann Radon Institute for Computational
and Applied Mathematics (RICAM)
Altenbergerstraße 69
A-4040 Linz, Austria

Abstract

In this paper, we study the mathematical imaging problem of optical diffraction tomography (ODT) for the scenario of a microscopic rigid particle rotating in a trap created, for instance, by acoustic or optical forces. Under the influence of the inhomogeneous forces the particle carries out a time-dependent smooth, but complicated motion described by a set of affine transformations. The rotation of the particle enables one to record optical images from a wide range of angles, which largely eliminates the “missing cone problem” in optics. This advantage, however, comes at the price that the rotation axis in this scenario is not fixed, but continuously undergoes some variations, and that the rotation angles are not equally spaced, which is in contrast to standard tomographic reconstruction assumptions. In the present work, we assume that the time-dependent motion parameters are known, and that the particle’s scattering potential is compatible with making the first order Born or Rytov approximation. We prove a Fourier diffraction theorem and derive novel backprojection formulae for the reconstruction of the scattering potential, which depends on the refractive index distribution inside the object, taking its complicated motion into account. This provides the basis for solving the ODT problem with an efficient non-uniform discrete Fourier transform.

1. INTRODUCTION

In *optical diffraction tomography* (ODT), see, for instance [2, 1, 3, 44, 27], the three-dimensional (3D) refractive index distribution of an object is constructed from optical measurements, i.e. from intensity images or from interferometric data, taken from different angles. The illumination directions are varied, for instance by active scanning or by means of a lenslet array as in

Fourier ptychography [45]. Alternatively, the object is embedded in a gel and rotated while the illumination direction is kept fixed. In either case, the light propagation directions utilized to solve the inverse problem from a set of images recorded from these directions are known. Moreover, typically the viewing directions are regularly distributed around a prevalent direction, which means that the viewing angles are restricted to a certain hardware-related interval. Depending on the width of this interval, the sampling in the Fourier plane remains incomplete, which leads to artefacts in the reconstruction, such as the well-known “missing cone artefact” in optics [30, 32, 43], which are exactly the geometrical figures plotted in Figure 2.

The present paper is motivated by the context of carrying out ODT on a trapped particle which is held in place by optical or acoustic forces [13]. We assume that these forces can be employed to induce rotations of the trapped particle in a controlled way, e.g. by using holographic optical tweezers with several spots or by standing ultrasound waves. This generally allows to view the particle from a wider range of directions than possible with illumination scans on a fixed object, and thus leads to more complete sampling in Fourier space and consequently to fewer artifacts. However, this comes at the price that the viewing directions are then not as regularly spaced as normally the case. Even more importantly, in optical or acoustic trapping the particle itself is not completely immobilized and the locally acting forces are typically inhomogeneous, so that the particle undergoes a time-dependent smooth, but complicated motion described by a set of affine transformations. In a real experimental situation, a video would be recorded and the parameters of the affine transformations, i.e. translation vector and rotation axis and angle at a given time, would have to be extracted at every sampling time by some suitable method. In this work we assume these parameters to be *known*. Apart from this, we assume that the particle can be described as a rigid body and that its center of mass is fixed, which means we do not have any translations but only rotation around the center of mass.

The concrete model, which we study in this paper, is based on a series of assumptions:

- (i) In a lens-less imaging configuration, the object is probed with *coherent* light, assumed as plane waves. The optical *field* (not just the intensity) is measured, either in reflection or in transmission. This means that the full optical amplitude and phase information has to be captured, for example interferometrically. Alternatively, we can consider data recorded by intensity measurements, where the phase has been determined by a phase-retrieval algorithm under suitable constraints [17].
- (ii) The scattering properties of the probe only *slightly deviate* from the background, meaning that linearized models assuming Born’s or Rytov’s approximation are valid. If these simplifications cannot be made, methods from *full waveform inversion* have to be considered, see, for instance [46]. This is not pursued here.
- (iii) Certain assumptions for the propagation of the light through the object have to be made, i.e. on the *forward model*: If the properties of object and optical set-up allow the imaging to be approximately given by geometric optics, then, mathematically, the problem becomes analogous to inverting the 3D X-ray transform, see [6]. In this case, the optical image resembles a projection image, and optical projection tomography can be used [40]. This is, for instance, fulfilled in low numerical aperture imaging of biological samples with sufficient amplitude contrast, with large structures on the scale of the optical wavelength and with limited refractive index contrast. For imaging with a higher numerical aperture objective, and/or for samples with small structures diffracting the light beams, deviations from geometrical optics are to be expected. In this situation diffraction models, see, for instance the work of Devaney [9, 11, 10] and [35], more accurately describing the propagation of the light through the sample, need to be considered. These models will be investigated in this

paper. Please note that all of these approaches still assume that first order Born or Rytov are valid, which means that the object cannot be strongly refracting or scattering.

- (iv) We assume that the motion of the particle has been estimated beforehand. We mention our work [15] for retrieving the motion parameters, which is applicable if the imaging of the sample is well approximated by *projections*, as described above. For motion estimation also the algorithms from single particle cryogenic electron microscopy (cryo-EM), see [25, 18, 7, 41, 47], can be used, which also serves as a prerequisite step for 3D-visualization also based on inverting the X-ray transform.

In this paper, we present an algorithm for 3D visualization of a single rigid object rotating around its center of mass. The mathematical model describing the optical experiment is a diffraction tomography model based on Born's or Rytov's simplifications. One challenge is the alignment of the exciting plane waves with the measurement plane. This particular setup therefore requires new mathematical research:

- (i) In contrast to the references on diffraction tomography mentioned above, in the envisaged tomography on levitated or trapped objects the measurement data is not uniformly sampled. To deal with such measurements, we use reconstruction formulae in the k-space, also known as Fourier-space, see Section 4.
- (ii) Born and Rytov approximations are also used in various kind of other applications such as seismics and ultrasound tomography, see [12, 9, 11, 10, 37, 36]. The frequency coverage on the reconstruction of the 3D Fourier transform of the scattering potential of the probe which is given by the measurement data, similarly as in Figure 2 below, have been observed there first [50, 34].
- (iii) For the numerical reconstruction, we propose the use of the inverse *Nonequispaced Discrete Fourier Transform* (NDFT), which can deal with the irregular motion considered here. For other regularization methods (such as variational ones) we refer to [32, 43].
- (iv) From a mathematical perspective it is important to consider the describing diffraction equations and backpropagation formulas in a rigorous distributional setting. Mathematically this sheds some new light on the reconstruction formulae.

The outline of this paper is as follows: In Section 2, we introduce the mathematical setting of diffraction tomography, and formulate the basic model based on Born's or Rytov's approximation for wave propagation. In Section 3, we state a rigorous proof of the Fourier diffraction theorem, which builds the foundation of our reconstruction formulae. Then, in Section 4, we derive a backpropagation reconstruction formula in k-space, which can take into account arbitrary (uncontrolled) rotations of the sample. Section 5 discusses the discretization of the backpropagation formula from the preceding section as well as an alternative reconstruction method based on the inverse NDFT. Section 6 shows numerical reconstructions, comparing the backpropagation formula with the inverse NDFT. The appendix Section 7 provides background information on distributions and Fourier analysis and some of the rather technical proofs.

2. CONCEPTUAL EXPERIMENT

In this section, we describe the experimental situation we have in mind when developing our tomographic reconstruction method for arbitrary object rotations and formulate the mathematical

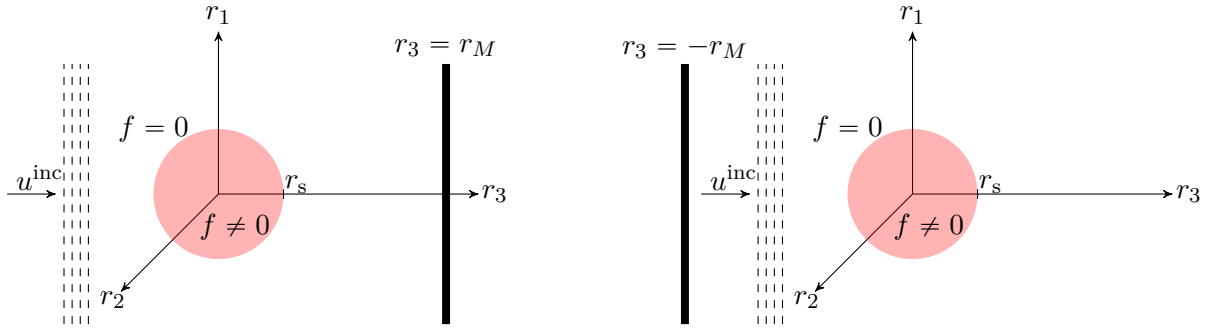


FIGURE 1. *Conceptual setup. The support of f lies entirely in \mathcal{B}_{r_s} . Left: Transmission imaging. Right: Reflection imaging.*

wave propagation models. A schematic overview of the set-up is given in [Figure 1](#).

The object we want to image tomographically is illuminated by a plane wave u^{inc} which propagates in direction $\mathbf{e}_3 = (0, 0, 1)^\top$ with wave number k_0 , that is

$$u^{\text{inc}}(\mathbf{r}) = e^{ik_0 r_3}. \quad (2.1)$$

Note that the wavelength λ of u^{inc} is related to the wave number via $k_0 = \frac{2\pi}{\lambda}$. The object is assumed to be enclosed by the open ball $\mathcal{B}_{r_s} \subset \mathbb{R}^3$ centered at $\mathbf{0}$ with radius r_s . In order to generate multiple illuminations of the object, it is rotated around its center of mass which is fixed at $\mathbf{0}$. The incident wave u^{inc} induces a scattered wave u^{sca} which is recorded in a plane at a distance from the object at $r_3 = r_M > r_s$ for transmission imaging and at $r_3 = -r_M < -r_s$ for reflection imaging, respectively.

By $n(\mathbf{r})$ we denote the refractive index of the object and by n_0 the constant refractive index of the background, respectively. The scattering properties of the object are characterized by the function

$$k(\mathbf{r}) = k_0 \frac{n(\mathbf{r})}{n_0}, \quad \text{for all } \mathbf{r} \in \mathbb{R}^3. \quad (2.2)$$

Note that k differs from k_0 only in \mathcal{B}_{r_s} . The function

$$f(\mathbf{r}) = k^2(\mathbf{r}) - k_0^2 \quad (2.3)$$

is referred to as the *scattering potential* [49] and will be the quantity which we set out to reconstruct from the measurements of the scattered waves. By construction we have

$$\text{supp}(f) \subseteq \mathcal{B}_{r_s} \subset (-r_s, r_s)^3. \quad (2.4)$$

The total field $u^{\text{tot}} = u^{\text{inc}} + u^{\text{sca}}$ satisfies the *reduced wave equation*

$$(\Delta + k^2)u^{\text{tot}} = 0, \quad (2.5)$$

while u^{inc} in turn fulfills the *Helmholtz equation*

$$(\Delta + k_0^2)u^{\text{inc}} = 0. \quad (2.6)$$

Next we will consider two simplifications of [Equation 2.5](#), the Born and Rytov approximations. While their underlying assumptions and physical validity are different, they may be analyzed within the same mathematical framework. More on the background and comparisons of the approximations can be found in [28, Chap. 6].

2.1. Born approximation. Inserting Equation 2.6 in Equation 2.5 together with some rearranging gives

$$-(\Delta + k_0^2)u^{\text{sca}} = f(u^{\text{sca}} + u^{\text{inc}}). \quad (2.7)$$

Neglecting u^{sca} in the right-hand side of Equation 2.7 (assuming that u^{sca} is small in comparison with u^{inc}), we obtain the *Born approximation*:

$$-(\Delta + k_0^2)u^{\text{Born}} = fu^{\text{inc}}. \quad (2.8)$$

2.2. Rytov approximation. We make the ansatz

$$u^{\text{tot}} = u^{\text{inc}} + u^{\text{sca}} = e^{\varphi^{\text{tot}}}, \quad u^{\text{inc}} = e^{ik_0 r_3} = e^{\varphi^{\text{inc}}} \quad \text{and} \quad \varphi^{\text{tot}} = \varphi^{\text{inc}} + \varphi^{\text{sca}}. \quad (2.9)$$

The calculations below should be considered formal. From Equation 2.9 it follows that

$$u^{\text{sca}} = u^{\text{tot}} - u^{\text{inc}} = e^{\varphi^{\text{tot}}} - e^{\varphi^{\text{inc}}} = e^{\varphi^{\text{inc}}} (e^{\varphi^{\text{sca}}} - 1). \quad (2.10)$$

We have

$$\nabla u^{\text{tot}} = u^{\text{tot}} \nabla \varphi^{\text{tot}} \quad \text{and} \quad \Delta u^{\text{tot}} = u^{\text{tot}} (\Delta \varphi^{\text{tot}} + (\nabla \varphi^{\text{tot}})^2), \quad (2.11)$$

where $(\nabla \varphi^{\text{tot}})^2 = \sum_{i=1}^3 \left(\frac{\partial \varphi^{\text{tot}}}{\partial r_i} \right)^2$ and similarly for u^{inc} . Then the Helmholtz Equation 2.6 and the reduced wave Equation 2.5 can be rewritten as

$$\begin{aligned} -k_0^2 &= \Delta \varphi^{\text{inc}} + (\nabla \varphi^{\text{inc}})^2, \\ -k^2 &= \Delta \varphi^{\text{tot}} + (\nabla \varphi^{\text{tot}})^2 = \Delta \varphi^{\text{inc}} + \Delta \varphi^{\text{sca}} + (\nabla \varphi^{\text{inc}} + \nabla \varphi^{\text{sca}})^2 \\ &= \Delta \varphi^{\text{inc}} + (\nabla \varphi^{\text{inc}})^2 + \Delta \varphi^{\text{sca}} + 2\nabla \varphi^{\text{inc}} \cdot \nabla \varphi^{\text{sca}} + (\nabla \varphi^{\text{sca}})^2, \\ -f &= \Delta \varphi^{\text{sca}} + 2\nabla \varphi^{\text{inc}} \cdot \nabla \varphi^{\text{sca}} + (\nabla \varphi^{\text{sca}})^2. \end{aligned} \quad (2.12)$$

For establishing the Rytov approximation, we consider

$$(\Delta + k_0^2)(u^{\text{inc}} \varphi^{\text{sca}}) = \varphi^{\text{sca}} \Delta u^{\text{inc}} + 2u^{\text{inc}} \nabla \varphi^{\text{inc}} \cdot \nabla \varphi^{\text{sca}} + u^{\text{inc}} \Delta \varphi^{\text{sca}} + k_0 u^{\text{inc}} \varphi^{\text{sca}},$$

which by Equation 2.6 becomes

$$(\Delta + k_0^2)(u^{\text{inc}} \varphi^{\text{sca}}) = (2\nabla \varphi^{\text{inc}} \cdot \nabla \varphi^{\text{sca}} + \Delta \varphi^{\text{sca}}) u^{\text{inc}}.$$

and by Equation 2.12 finally

$$-(\Delta + k_0^2)(u^{\text{inc}} \varphi^{\text{sca}}) = \left(f + (\nabla \varphi^{\text{sca}})^2 \right) u^{\text{inc}}. \quad (2.13)$$

Neglecting $(\nabla \varphi^{\text{sca}})^2$ in Equation 2.13, we obtain the *Rytov approximation* φ^{Rytov} :

$$-(\Delta + k_0^2)(u^{\text{inc}} \varphi^{\text{Rytov}}) = fu^{\text{inc}}. \quad (2.14)$$

Comparing the Born and Rytov approximations, we find their relation

$$u^{\text{Born}} = u^{\text{inc}} \varphi^{\text{Rytov}}.$$

Therefore, it is sufficient to concentrate on the Born approximation. For simplicity of notation, we set $u^{\text{Born}} = u$ from now on.

3. FOURIER DIFFRACTION THEOREM

The Fourier diffraction theorem, see [28, Sect. 6.3], [37, Thm. 3.1] or [49], is the basis for reconstruction formulae in diffraction tomography, as it relates the 2D Fourier transform of the measurements to the 3D Fourier transform of the scattering potential. In this section, we establish a version of the Fourier diffraction theorem that suits the experimental setup described in Section 2.

Under Born's approximation, the relation between the scattered wave u and the scattering potential f is governed by Equation 2.8. We assume further that u satisfies the *Sommerfeld radiation condition*

$$\lim_{s \rightarrow \infty} \max_{\|\mathbf{r}\|=s} \|\mathbf{r}\| \left(\frac{\partial}{\partial \mathbf{r}} u(\mathbf{r}) - ik_0 u(\mathbf{r}) \right) = 0,$$

where $\frac{\partial}{\partial \mathbf{r}}$ denotes the directional derivative. Physically speaking, u is an outgoing wave.

To formulate the diffraction theorem, we need the following notation. We set

$$\kappa = \kappa(k_1, k_2) := \begin{cases} \sqrt{k_0^2 - k_1^2 - k_2^2}, & k_1^2 + k_2^2 \leq k_0^2, \\ i\sqrt{k_1^2 + k_2^2 - k_0^2}, & k_1^2 + k_2^2 > k_0^2. \end{cases} \quad (3.1)$$

Furthermore, $H_{r_3} : \mathbb{R}^3 \rightarrow \mathbb{R}$ denotes the *Heaviside function* in the third coordinate centered at r_3 , that is,

$$H_{r_3}(s_1, s_2, s_3) := \begin{cases} 0 & \text{if } s_3 < r_3, \\ 1 & \text{otherwise.} \end{cases}$$

Finally, we denote by $\mathcal{F}_{1,2}$ the *partial Fourier transform* which is taken with respect to the first two components, by $\mathcal{D}'(\mathbb{R}^3)$ the space of distributions and by $S'(\mathbb{R}^3)$, the space of tempered distributions. Further background material on Fourier transforms, convolutions and distributions is given in Section 7.1 and Section 7.2 in the appendix. Then we can establish the following theorem whose proof is given in Section 7.3.

Theorem 3.1 *Let $k_0 > 0$ and $g \in L^p(\mathbb{R}^3)$, $p > 1$, with $\text{supp}(g) \subset \mathcal{B}_r$ for some $r > 0$. Suppose that the function u is the solution of*

$$\Delta u + k_0^2 u = -g \quad (3.2)$$

which satisfies the Sommerfeld radiation condition. Then, we can identify the distribution $\mathcal{F}_{1,2}u$ almost everywhere with the following locally integrable function

$$\mathcal{F}_{1,2}u(k_1, k_2, r_3) = \sqrt{\frac{\pi}{2}} \frac{i}{\kappa} \left(e^{i\kappa r_3} \mathcal{F}((1 - H_{r_3})g)(k_1, k_2, \kappa) + e^{-i\kappa r_3} \mathcal{F}(H_{r_3}g)(k_1, k_2, -\kappa) \right). \quad (3.3)$$

Remark 3.2 (i) By the fundamental lemma of variational calculus of du Bois–Reymond, see [20, Lem. 3.2], Equation 3.3 is equivalent with equality of both functions considered as distributions in $\mathcal{D}'(\mathbb{R}^3)$. Note that the identification of Equation 3.3 does not hold, in general, for $\mathcal{F}_{1,2}u$ as an element of $S'(\mathbb{R}^3)$ since the right-hand side is not guaranteed to be polynomially bounded as $\|(k_1, k_2, r_3)\| \rightarrow \infty$, compare with Example 7.7.

(ii) Recall further that κ is imaginary for $k_1^2 + k_2^2 > k_0^2$. In this case, in Equation 3.3, we have to consider the analytic continuations of $\mathcal{F}((1 - H_{r_3})g)$ and $\mathcal{F}(H_{r_3}g)$ to \mathbb{C}^3 .

The theorem implies the following Fourier diffraction result for our setting, see Figure 1.

Corollary 3.3 *Assume that*

- (i) *the scattering potential of the probe is given by $f \in L^p$, $p > 1$, where $\text{supp}(f) \subset \mathcal{B}_{r_s}$, $0 < r_s < r_M$,*
- (ii) *the incident field is a plane wave $u^{\text{inc}}(\mathbf{r}) = e^{ik_0 r_3}$,*
- (iii) *the Born approximation is valid for the scattered field u and u satisfies the Sommerfeld radiation condition,*
- (iv) *the scattered field u is measured at the plane $r_3 = r_M$ (transmission imaging) or $r_3 = -r_M$ (reflection imaging).*

Then

$$\mathcal{F}_{1,2}u(k_1, k_2, \pm r_M) = \sqrt{\frac{\pi}{2}} \frac{ie^{ik_0 r_M}}{\kappa} \mathcal{F}f(k_1, k_2, \pm\kappa - k_0) \quad (3.4)$$

for all $k_1, k_2 \in \mathbb{R}$ satisfying $k_1^2 + k_2^2 \neq k_0^2$.

Proof: Assuming validity of the Born approximation, the scattered wave u satisfies [Equation 2.8](#). According to [Theorem 3.1](#) with $g = fu^{\text{inc}}$, we obtain

$$\begin{aligned} \mathcal{F}_{1,2}u(k_1, k_2, r_3) &= \frac{i\sqrt{\pi}}{\kappa\sqrt{2}} \left(e^{ik_0 r_3} \mathcal{F}((1 - H_{r_3})fu^{\text{inc}})(k_1, k_2, \kappa) + e^{-ik_0 r_3} \mathcal{F}(H_{r_3}fu^{\text{inc}})(k_1, k_2, -\kappa) \right) \\ &= \frac{i\sqrt{\pi}}{\kappa\sqrt{2}} \left(e^{ik_0 r_3} \mathcal{F}((1 - H_{r_3})f)(k_1, k_2, \kappa - k_0) + e^{-ik_0 r_3} \mathcal{F}(H_{r_3}f)(k_1, k_2, -\kappa - k_0) \right), \end{aligned}$$

where we have exploited the specific form of the incident wave u^{inc} . Finally, for transmission imaging, we have $r_3 = r_M$, so that $H_{r_M}f = 0$ and $(1 - H_{r_M})f = f$. Similarly, for reflection imaging, where $r_3 = -r_M$, we obtain $(1 - H_{-r_M})f = 0$ and $H_{-r_M}f = f$. \square

Remark 3.4 Even though, mathematically, [Equation 3.4](#) holds as long as $k_1^2 + k_2^2 \neq k_0^2$, physically speaking the spatial frequencies with $k_1^2 + k_2^2 > k_0^2$ do not contribute to the measurements. Therefore, without rotation of the object, the measurements in both transmission and reflection imaging provide access to the scattering potential f on a hemisphere

$$\{(k_1, k_2, \pm\kappa - k_0)^\top : k_1, k_2 \in \mathbb{R}, k_1^2 + k_2^2 < k_0^2\}$$

in k-space. The two hemispheres are depicted in [Figure 2](#).

4. BACKPROPAGATION FORMULAE

According to the Fourier diffraction theorem, illumination of the object from a single direction provides access to the scattering potential on a *surface* in k-space. If the probe is rotated continuously, however, we can obtain knowledge of $\mathcal{F}f$ in a *volume* \mathcal{Y} , see [Figure 3](#) for an illustration of such a volume. Consequently, an approximation of the scattering potential that incorporates all the available information can be found by means of Fourier inversion

$$f(\mathbf{r}) \approx (2\pi)^{-\frac{3}{2}} \int_{\mathcal{Y}} e^{i\mathbf{y} \cdot \mathbf{r}} \mathcal{F}f(\mathbf{y}) d\mathbf{y}.$$

The reconstruction formula for our setting is made precise in [Theorem 4.1](#) and [Lemma 4.2](#) below.

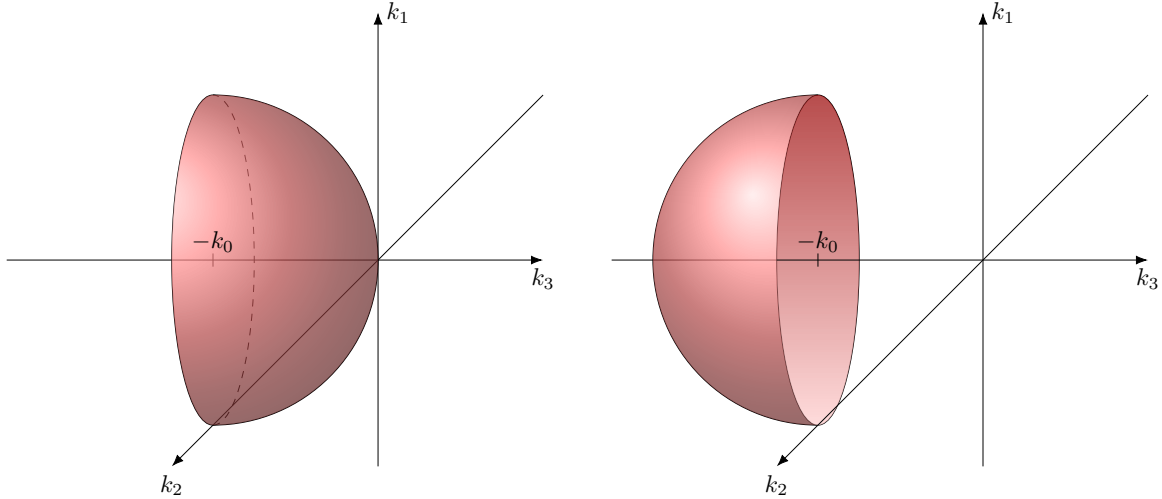


FIGURE 2. Accessible points in k -space for transmission imaging (left) and reflection imaging (right).

We assume that the scattering object undergoes a rotation with varying rotation axis. Therefore, if the function $\mathbf{n} = \mathbf{n}(t) : [0, L] \rightarrow \mathbb{S}^2$ describes the orientation of this axis and $\alpha = \alpha(t) : [0, L] \rightarrow \mathbb{R}$ is the corresponding angle, then the rotation can be represented by the matrix

$$R_{\mathbf{n},\alpha}^\top := \begin{pmatrix} n_1^2(1-c) + c & n_1n_2(1-c) - n_3s & n_1n_3(1-c) + n_2s \\ n_1n_2(1-c) + n_3s & n_2^2(1-c) + c & n_2n_3(1-c) - n_1s \\ n_1n_3(1-c) - n_2s & n_2n_3(1-c) + n_1s & n_3^2(1-c) + c \end{pmatrix},$$

where $\mathbf{n} = (n_1, n_2, n_3)^\top$, $c := \cos \alpha$ and $s := \sin \alpha$. Note that we follow the convention of describing the rotation of the object by the transpose $R_{\mathbf{n},\alpha}^\top$. Therefore, the scattering potential of the rotated object is given by $f \circ R_{\mathbf{n},\alpha}$.

Next, denote by u_t , $0 \leq t \leq L$, the wave scattered by the rotated potential $f \circ R_{\mathbf{n}(t),\alpha(t)}$. Under Born's approximation, it satisfies

$$\Delta u_t + k_0^2 u_t = -u^{\text{inc}} f \circ R_{\mathbf{n}(t),\alpha(t)}.$$

The full set of measurements in the transmission and reflection setup, respectively, is then given by

$$u_t(r_1, r_2, \pm r_M), \quad r_1, r_2 \in \mathbb{R}, \quad 0 \leq t \leq L, \quad (4.1)$$

and, according to [Corollary 3.3](#), it is related to the scattering potential f via

$$\mathcal{F}_{1,2} u_t(k_1, k_2, \pm r_M) = \sqrt{\frac{\pi}{2}} \frac{ie^{i\kappa r_M}}{\kappa} \mathcal{F} f (R_{\mathbf{n}(t),\alpha(t)}(k_1, k_2, \pm \kappa - k_0)^\top). \quad (4.2)$$

Next, let

$$\mathcal{U} := \{(k_1, k_2, t) \in \mathbb{R}^3 : k_1^2 + k_2^2 < k_0^2, 0 \leq t \leq L\}$$

be the set where [Equation 4.2](#) is valid and can be used for reconstruction purposes, recall [Remark 3.4](#). Moreover, the map that traces out the accessible domain in k -space is denoted by

$$T_\pm : \mathcal{U} \rightarrow \mathbb{R}^3, \quad T_\pm(k_1, k_2, t) := R_{\mathbf{n}(t),\alpha(t)}(k_1, k_2, \pm \kappa - k_0)^\top. \quad (4.3)$$

In the reconstruction formula below we have to take into account the number of times a point \mathbf{y} in k -space is covered by T_\pm . This number, sometimes referred to as *Banach indicatrix* of

T_{\pm}^{-1} , will be denoted by $\text{Card}(T_{\pm}^{-1}(\mathbf{y}))$, where $\text{Card}(A)$ is the cardinality of a set A . Finally, the approximation to f we wish to reconstruct is

$$f_{\text{bp}}^{\pm}(\mathbf{r}) := (2\pi)^{-\frac{3}{2}} \int_{T_{\pm}(\mathcal{U})} e^{i\mathbf{y}\cdot\mathbf{r}} \mathcal{F}f(\mathbf{y}) d\mathbf{y}. \quad (4.4)$$

The set $T_{\pm}(\mathcal{U})$ will be referred to as the *frequency coverage* or *k-space coverage* of the experimental setup.

Theorem 4.1 *Let the assumptions of Corollary 3.3 be satisfied. In addition, assume that $\alpha \in C^1[0, L]$ and $\mathbf{n} \in C^1([0, L], \mathbb{S}^2)$. Then, for all $\mathbf{r} \in \mathbb{R}^3$,*

$$f_{\text{bp}}^{\pm}(\mathbf{r}) = \frac{-i}{2\pi^2} \int_{\mathcal{U}} e^{iT_{\pm}(k_1, k_2, t)\cdot\mathbf{r}} \mathcal{F}_{1,2}u_t(k_1, k_2, \pm r_M) \frac{\kappa e^{-i\kappa r_M} |\nabla T_{\pm}(k_1, k_2, t)|}{\text{Card}(T_{\pm}^{-1}(T_{\pm}(k_1, k_2, t)))} d(k_1, k_2, t), \quad (4.5)$$

where $|\nabla T_{\pm}|$ is the magnitude of the Jacobian determinant of T_{\pm} .

Proof: First, we show that $\text{Card}(T_{\pm}^{-1})$ is finite at almost every point in the range of T_{\pm} . By Lemma 4.2, we have $|\nabla T_{\pm}| \in L^1(\mathcal{U})$. Applying a change of variables that takes into account the potential noninjectivity of T_{\pm} , see [5, Thm. 5.8.30], gives $\int_{T_{\pm}(\mathcal{U})} \text{Card}(T_{\pm}^{-1}) d\mathbf{y} = \int_{\mathcal{U}} |\nabla T_{\pm}| d\mathbf{y}$. It follows that $\text{Card}(T_{\pm}^{-1}(\mathbf{y})) < \infty$ for almost every $\mathbf{y} \in T_{\pm}(\mathcal{U})$.

Next, we can write

$$f_{\text{bp}}^{\pm}(\mathbf{r}) = (2\pi)^{-\frac{3}{2}} \int_{T_{\pm}(\mathcal{U})} e^{i\mathbf{y}\cdot\mathbf{r}} \mathcal{F}f(\mathbf{y}) \frac{\text{Card}(T_{\pm}^{-1}(\mathbf{y}))}{\text{Card}(T_{\pm}^{-1}(\mathbf{y}))} d\mathbf{y},$$

since $\text{Card}(T_{\pm}^{-1})$ vanishes nowhere and is finite almost everywhere. Applying [5, Thm. 5.8.30] once again, where the function to be integrated is $\mathbf{y} \mapsto e^{i\mathbf{y}\cdot\mathbf{r}} \mathcal{F}f(\mathbf{y}) / \text{Card}(T_{\pm}^{-1}(\mathbf{y}))$, gives

$$f_{\text{bp}}^{\pm}(\mathbf{r}) = (2\pi)^{-\frac{3}{2}} \int_{\mathcal{U}} e^{iT_{\pm}(k_1, k_2, t)\cdot\mathbf{r}} \mathcal{F}f(T_{\pm}(k_1, k_2, t)) \frac{|\nabla T_{\pm}(k_1, k_2, t)|}{\text{Card}(T_{\pm}^{-1}(T_{\pm}(k_1, k_2, t)))} d(k_1, k_2, t). \quad (4.6)$$

The assertion now follows after using Equation 4.2 to express $\mathcal{F}f$ in terms of the measurements. \square

In order to actually use the reconstruction formula (4.5), it remains to calculate the Jacobian determinant $|\nabla T_{\pm}|$ as well as the Banach indicatrix $\text{Card}(T_{\pm}^{-1})$. While the former is carried out in Lemma 4.2, the latter is quite a challenging task in general. However, in the remainder of this section we identify special cases for which we can determine $\text{Card}(T_{\pm}^{-1})$.

Lemma 4.2 *For $\alpha \in C^1[0, L]$ and $\mathbf{n} \in C^1([0, L], \mathbb{S}^2)$, the Jacobian determinant of T_{\pm} is given by*

$$|\nabla T_{\pm}(k_1, k_2, t)| = \frac{k_0}{\kappa} \left| \left((1 - \cos \alpha) (n_3 \mathbf{n}' \cdot \mathbf{h} - n_3' \mathbf{n} \cdot \mathbf{h}) - n_3 \mathbf{n} \cdot (\mathbf{n}' \times \mathbf{h}) \sin \alpha \right) - \alpha' (n_1 k_2 - n_2 k_1) + (\mathbf{n} \cdot \mathbf{h}) (n_1 n_2' - n_2 n_1') \sin \alpha \right|, \quad (4.7)$$

where $\mathbf{h} := (k_1, k_2, \pm\kappa - k_0)^{\top}$. In particular $|\nabla T_{\pm}| \in L^1(\mathcal{U})$.

The proof of this lemma is postponed until Section 7.4.

For rotation axes independent of t the Jacobian determinant of T_{\pm} simplifies considerably. Moreover, the Banach indicatrix is constant almost everywhere.

¹In Computerized Tomography (CT) the Banach indicatrix is called Crofton symbol (see for instance [33]).

Corollary 4.3 *Let the assumptions of [Theorem 4.1](#) be satisfied. If $\mathbf{n}'(t) = \mathbf{0}$, then*

$$|\nabla T_{\pm}(k_1, k_2, t)| = \frac{k_0 |\alpha'(t)| |n_2 k_1 - n_1 k_2|}{\kappa}. \quad (4.8)$$

If in addition $\mathbf{n} \neq \mathbf{e}_3$ and α is strictly increasing with $\alpha(0) = 0$ and $\alpha(L) = 2\pi$, then

$$\text{Card}(T_{\pm}^{-1}(T_{\pm}(k_1, k_2, t))) = 2$$

for almost every $(k_1, k_2, t) \in \mathcal{U}$.

Proof: [Equation 4.8](#) is a direct consequence of [Equation 4.7](#). It remains to show the second statement. Let $(\hat{k}_1, \hat{k}_2, \hat{t}) \in \mathcal{U}$ be given. We want to find the number of points $(k_1, k_2, t) \in \mathcal{U}$ which satisfy

$$T_{\pm}(k_1, k_2, t) = T_{\pm}(\hat{k}_1, \hat{k}_2, \hat{t}). \quad (4.9)$$

First, we point out that there can be no $t \neq \hat{t}$ such that

$$T_{\pm}(\hat{k}_1, \hat{k}_2, t) = T_{\pm}(\hat{k}_1, \hat{k}_2, \hat{t}),$$

unless $T_{\pm}(\hat{k}_1, \hat{k}_2, \hat{t})$ lies on the rotation axis or $\hat{t} \in \{0, L\}$. These cases, however, correspond to a subset $\mathcal{V} \subset \mathcal{U}$ of measure zero.

Thus we look for $(k_1, k_2) \neq (\hat{k}_1, \hat{k}_2)$. Denote a general point on the hemisphere by $\mathbf{h}^{\pm} = \mathbf{h}^{\pm}(k_1, k_2) := (k_1, k_2, \pm\kappa - k_0)^{\top}$ and set $\hat{\mathbf{h}}^{\pm} := \mathbf{h}^{\pm}(\hat{k}_1, \hat{k}_2)$. Since T_{\pm} is the composition of \mathbf{h}^{\pm} with a rotation and rotations preserve the lengths of vectors, we deduce from [Equation 4.9](#) that

$$\|\mathbf{h}^{\pm}\| = \|\hat{\mathbf{h}}^{\pm}\|. \quad (4.10)$$

Calculating these norms shows that $\kappa(k_1, k_2) = \kappa(\hat{k}_1, \hat{k}_2)$ and that

$$k_1^2 + k_2^2 = \hat{k}_1^2 + \hat{k}_2^2. \quad (4.11)$$

Furthermore, the rotation $R_{\mathbf{n}, \alpha}$ does not affect the vector component in the direction of the rotation axis \mathbf{n} , that is,

$$\mathbf{h}^{\pm} \cdot \mathbf{n} = R_{\mathbf{n}, \alpha(t)} \mathbf{h}^{\pm} \cdot \mathbf{n} = R_{\mathbf{n}, \alpha(\hat{t})} \hat{\mathbf{h}}^{\pm} \cdot \mathbf{n} = \hat{\mathbf{h}}^{\pm} \cdot \mathbf{n} \quad (4.12)$$

and consequently

$$0 = \mathbf{n} \cdot (\mathbf{h}^{\pm} - \hat{\mathbf{h}}^{\pm}) = n_1(k_1 - \hat{k}_1) + n_2(k_2 - \hat{k}_2).$$

Since, by assumption, $n_1^2 + n_2^2 \neq 0$, there exists $\lambda \in \mathbb{R}$ such that $k_1 - \hat{k}_1 = -\lambda n_2$ and $k_2 - \hat{k}_2 = \lambda n_1$. Hence, $(k_1, k_2) = (\hat{k}_1 - \lambda n_2, \hat{k}_2 + \lambda n_1)$. Now we conclude from [Equation 4.11](#) that

$$0 = \lambda^2(n_1^2 + n_2^2) + 2\lambda(\hat{k}_2 n_1 - \hat{k}_1 n_2),$$

which has the two solutions $\lambda_1 = 0$ and $\lambda_2 = 2(\hat{k}_2 n_1 - \hat{k}_1 n_2)/(n_1^2 + n_2^2)$. The former corresponds to $(k_1, k_2) = (\hat{k}_1, \hat{k}_2)$ and the latter to a reflection of (\hat{k}_1, \hat{k}_2) across the line passing through the origin with direction (n_1, n_2) . We can ignore the possibility that the two solutions coincide, as this corresponds to a set of measure zero.

It remains to count the $t \in [0, L]$ which satisfy

$$T_{\pm}(\hat{k}_1 - \lambda_2 n_2, \hat{k}_2 + \lambda_2 n_1, t) = T_{\pm}(\hat{k}_1, \hat{k}_2, \hat{t}). \quad (4.13)$$

[Equation 4.10](#) and [Equation 4.12](#) imply that during rotation $\hat{\mathbf{h}}^{\pm}$ and $\mathbf{h}^{\pm}(\hat{k}_1 - \lambda_2 n_2, \hat{k}_2 + \lambda_2 n_1)$ move along the same circle around the rotation axis. Since, by assumption, the range of α is $[0, 2\pi]$, both points on the hemisphere make a full turn. So there must be at least one t satisfying [Equation 4.13](#). But since α is also bijective, there is exactly one such t . Thus we have shown that for almost every $(\hat{k}_1, \hat{k}_2, \hat{t}) \in \mathcal{U}$ there is exactly one other point (k_1, k_2, t) such that [Equation 4.9](#) holds. Therefore $\text{Card}(T_{\pm}^{-1}(T_{\pm}(\hat{k}_1, \hat{k}_2, \hat{t}))) = 2$ almost everywhere in \mathcal{U} . \square

Let us consider a simple example which is also treated in the numerical part.

Example 4.4 (Full uniform rotation around the r_1 -axis) We consider rotation around the r_1 -axis with rotation matrix

$$R_{\mathbf{e}_1, \alpha}^\top = \begin{pmatrix} 1 & 0 & 0 \\ 0 & \cos \alpha & -\sin \alpha \\ 0 & \sin \alpha & \cos \alpha \end{pmatrix}$$

and $\alpha(t) = t$, $t \in [0, 2\pi]$. Instead of t we write α below. From [Corollary 4.3](#) it follows that

$$f_{\text{bp}}^\pm(\mathbf{r}) = \frac{-ik_0}{4\pi^2} \int_{\mathcal{U}} e^{i(R_{\mathbf{e}_1, \alpha} \mathbf{h}^\pm \cdot \mathbf{r} - \kappa r_M)} \mathcal{F}_{1,2} u_\alpha(k_1, k_2, \pm r_M) |k_2| d(k_1, k_2, \alpha), \quad (4.14)$$

where $\mathbf{h}^\pm := (k_1, k_2, \pm\kappa - k_0)^\top$.

We want to illustrate the corresponding sets $T_\pm(\mathcal{U})$. Consider $\mathbf{y} \in T_+(\mathcal{U})$, i.e. $\mathbf{y} = (y_1, y_2, y_3)^\top = R_{\mathbf{e}_1, \alpha}(k_1, k_2, \kappa - k_0)^\top$ where $k_1^2 + k_2^2 < k_0^2$ and $0 \leq \alpha \leq 2\pi$. Then, it holds that $y_1 = k_1$ and

$$\begin{aligned} y_2^2 + y_3^2 &= k_2^2 + (\kappa - k_0)^2 = k_2^2 + k_0^2 - k_1^2 - k_2^2 - 2\kappa k_0 + k_0^2 \\ &= 2k_0^2 - 2k_0 \sqrt{k_0^2 - k_1^2 - k_2^2} - k_1^2. \end{aligned}$$

Since $k_2^2 \in [0, k_0^2 - k_1^2)$, this implies

$$\begin{aligned} y_2^2 + y_3^2 &< 2k_0^2 - y_1^2, \\ y_2^2 + y_3^2 &\geq 2k_0^2 - 2k_0 \sqrt{k_0^2 - y_1^2} - y_1^2 = \left(k_0 - \sqrt{k_0^2 - y_1^2}\right)^2. \end{aligned}$$

The first equation can be rewritten as $\|\mathbf{y}\|^2 < 2k_0^2$, while the second equation gives

$$\begin{aligned} \|(y_2, y_3)\| &\geq k_0 - \sqrt{k_0^2 - y_1^2} \\ k_0 - \|(y_2, y_3)\| &\leq \sqrt{k_0^2 - y_1^2}. \end{aligned}$$

Noting that $k_0 - \|(y_2, y_3)\| > -\sqrt{k_0^2 - y_1^2}$ and taking the square, we get $(\|(y_2, y_3)\| - k_0)^2 + y_1^2 \leq k_0^2$. In summary, we see that

$$T_+(\mathcal{U}) = \{\mathbf{y} \in \mathbb{R}^3 : \|\mathbf{y}\|^2 < 2k_0^2, (\|(y_2, y_3)\| - k_0)^2 + y_1^2 \leq k_0^2\}, \quad (4.15)$$

which is displayed in [Figure 3](#). Similar considerations for $T_-(\mathcal{U})$ show that this set together with $T_+(\mathcal{U})$ generates a solid horn torus of radius k_0 , see [Figure 3](#) right. Finally we point out that a rotation around any other axis in the r_1 - r_2 -plane leads to a k-space coverage $T_\pm(\mathcal{U})$ which is a rotated version of the one displayed in [Figure 3](#).

Remark 4.5 (Maximal and minimal k-space coverage) Subsequent rotations about two orthogonal axes in the r_1 - r_2 -plane generate a radially symmetric k-space coverage according to [Figure 4](#). This is the maximal coverage that can be obtained within the experimental setup. In contrast, the rotation around the r_3 -axis does not provide additional information in k-space, recall [Figure 2](#).

In the previous examples, the rotation axis \mathbf{n} was kept constant. In the following, we consider a moving rotation axis $\mathbf{n}(t)$, $t \in [0, 2\pi]$, in the setup of transmission imaging.

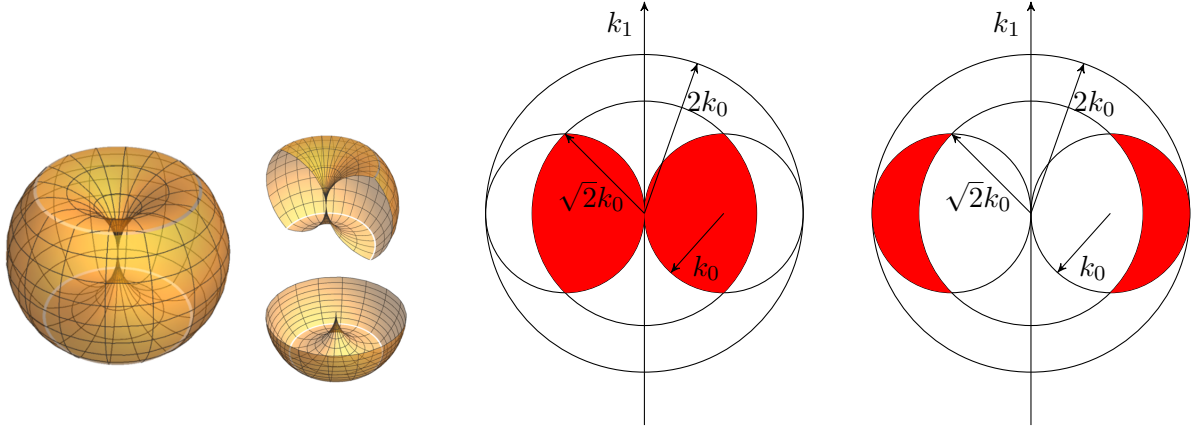


FIGURE 3. Frequency coverage $T_{\pm}(\mathcal{U})$ for a full rotation about the r_1 -axis. Left: 3D visualization of $T_+(\mathcal{U})$ (transmission imaging). Middle: Cross section of $T_+(\mathcal{U})$. Right: Cross section of $T_-(\mathcal{U})$ (reflection imaging).

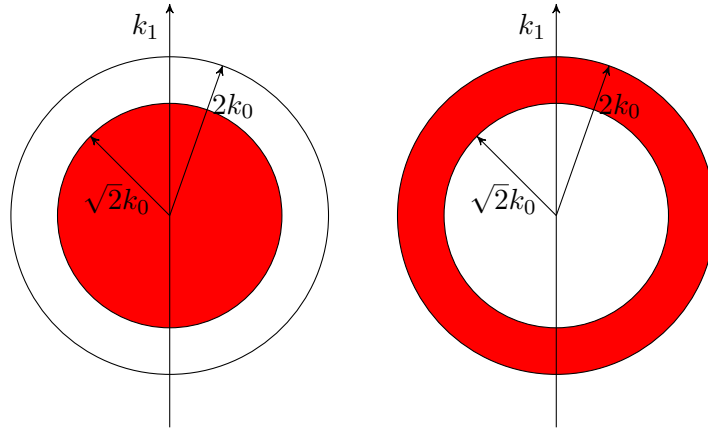


FIGURE 4. Frequency coverage for subsequent rotations around two orthogonal axes in the r_1 - r_2 plane. Left: Cross section of transmission imaging. Right: Cross section of reflection imaging.

Proposition 4.6 *Let $\mathbf{n} \in C^1([0, 2\pi], \mathbb{S}^2)$ and $\alpha \in C^1[0, L]$. We denote the trajectory of $\mathbf{e}_3 = (0, 0, 1)^\top$ under T_+ by*

$$\mathbf{e}(t) := R_{\mathbf{n}(t), \alpha(t)} \mathbf{e}_3, \quad t \in [0, L].$$

Let $\mathbf{y} \in \mathbb{R}^3$ with $\|\mathbf{y}\| < \sqrt{2}k_0$. Then, there exists $(k_1, k_2, t) \in \mathcal{U}$ with $T_+(k_1, k_2, t) = \mathbf{y}$ if and only if

$$\mathbf{y} \cdot \mathbf{e}(t) = -\frac{\|\mathbf{y}\|^2}{2k_0}. \quad (4.16)$$

Moreover, $\text{Card}(T_+^{-1}(\mathbf{y}))$ equals the number of solutions $t \in [0, L]$ of Equation 4.16.

Proof: Assume that there exists $(k_1, k_2, t) \in \mathcal{U}$ such that $\mathbf{y} = T_+(k_1, k_2, t) = R_{\mathbf{n}(t), \alpha(t)} \mathbf{h}$ with $\mathbf{h} = (k_1, k_2, \kappa - k_0)$. Since the norm is invariant under rotations, it holds that

$$\|\mathbf{y}\|^2 = \|\mathbf{h}\|^2 = 2k_0(k_0 - \kappa), \quad (4.17)$$

which implies that $\kappa = \sqrt{k_0^2 - k_1^2 - k_2^2}$ depends only on $\|\mathbf{y}\|$ and, by the invariance of the scalar product under the rotation $R_{\mathbf{n}(t), -\alpha(t)}$, it follows from Equation 4.17 that

$$\mathbf{y} \cdot \mathbf{e}(t) = \mathbf{h} \cdot \mathbf{e}_3 = h_3 = \kappa - k_0 = -\frac{\|\mathbf{y}\|^2}{2k_0},$$

which shows Equation 4.16.

Conversely, let $\mathbf{y} \in \mathbb{R}^3$ with $\|\mathbf{y}\| < \sqrt{2}k_0$, and let t satisfy [Equation 4.16](#). Set $\mathbf{k} = (k_1, k_2, k_3)^\top := R_{\mathbf{n}(t), -t}\mathbf{y}$. We show that $(k_1, k_2, t) \in \mathcal{U}$ and $T_+(k_1, k_2, t) = \mathbf{y}$, i.e., that $k_3 = \sqrt{k_0^2 - k_1^2 - k_2^2} - k_0$. We have by [Equation 4.16](#) and the invariance of the scalar product and vector lengths with respect to rotations

$$k_3 = \mathbf{k} \cdot \mathbf{e}_3 = \mathbf{y} \cdot \mathbf{e}(t) = \frac{-\|\mathbf{y}\|^2}{2k_0} = \frac{-\|\mathbf{k}\|^2}{2k_0} > -k_0$$

so that $k_3 + k_0 > 0$. Moreover, the above equation implies that

$$(k_3 + k_0)^2 = -k_1^2 - k_2^2 + k_0^2. \quad (4.18)$$

Thus, $k_1^2 + k_2^2 < k_0^2$, so that $(k_1, k_2, t) \in \mathcal{U}$. Taking the square root in [Equation 4.18](#), we obtain the desired form of k_3 . Since, for fixed t , the map $(\tilde{k}_1, \tilde{k}_2) \mapsto T_+(\tilde{k}_1, \tilde{k}_2, t)$ is one-to-one, we have shown the assertion. \square

Example 4.7 (Half rotation around the r_1 -axis) We consider the same fixed rotation axis as in [Example 4.4](#), but we restrict the angle $\alpha(t) = t$, $t \in [0, \pi]$. In what follows, we show that the Banach indicatrix $\text{Card}(T_+^{-1}(\cdot))$ takes different values on sets of positive measure, see [Figure 5](#).

Let $\mathbf{y} \in T_+(\mathcal{U}) \setminus \{\mathbf{0}\}$. Since $T_+(\mathcal{U})$ is a subset of the \mathbf{k} -space coverage for the full rotation, [Equation 4.15](#) shows that $\|\mathbf{y}\|^2 < 2k_0^2$ and $(\|(y_2, y_3)\| - k_0)^2 + y_1^2 \leq k_0^2$, which yields $\|\mathbf{y}\|^2 \leq 2k_0\sqrt{y_2^2 + y_3^2}$. By [Proposition 4.6](#), the Banach indicatrix $\text{Card}(T_+^{-1}(\mathbf{y}))$ is equal to the number of solutions $t \in [0, \pi]$ of

$$y_2 \sin t + y_3 \cos t = -\frac{\|\mathbf{y}\|^2}{2k_0}. \quad (4.19)$$

Let us denote the left side by

$$\psi(t) := y_2 \sin t + y_3 \cos t, \quad t \in [0, \pi].$$

If $y_2, y_3 \neq 0$, the derivative $\psi'(t) = y_2 \cos t - y_3 \sin t$ has only one zero $t_0 = \arctan \frac{y_2}{y_3}$ in $[0, \pi]$, where we use the branch of the arctangent with range $[0, \pi)$. If $y_3 = 0$ and $y_2 \neq 0$, then ψ' has the unique zero $t_0 = \frac{\pi}{2}$, which comes along with setting $\arctan \frac{y_2}{0} = \frac{\pi}{2}$. If $y_2 = 0$ and $y_3 \neq 0$, then ψ is monotone on $[0, \pi]$ and thus [Equation 4.19](#) has one solution. If $y_2 = y_3 = 0$, also $y_1 = 0$ and thus there are infinitely many solutions.

In the case $y_2 < 0$, we see that the unique zero $t_0 \in [0, \pi]$ of ψ' fulfills $\sin t_0 = y_2\sqrt{y_2^2 + y_3^2}$ and $\cos t_0 = y_3\sqrt{y_2^2 + y_3^2}$. Then we obtain $\psi(t_0) = -\sqrt{y_2^2 + y_3^2} < 0$. The second derivative is $\psi''(t) = -\psi(t)$ and hence $\psi''(t_0) > 0$. Together with the continuity of ψ' , this implies that ψ decreases on $[0, t_0]$ and increases on $[t_0, \pi]$. We have the two local maxima $\psi(0) = y_3$ and $\psi(\pi) = -y_3$ and the minimum $\psi(t_0) = -\sqrt{y_2^2 + y_3^2}$. Hence, [Equation 4.19](#) has two solutions if $-\frac{\|\mathbf{y}\|^2}{2k_0} \leq -|y_3|$ and otherwise one solution if $0 > -\frac{\|\mathbf{y}\|^2}{2k_0} > -|y_3|$. Note that we have already seen that $\|\mathbf{y}\|^2 \leq 2k_0\sqrt{y_2^2 + y_3^2}$.

An analogous consideration for $y_2 > 0$ shows that ψ has its maximum $\sqrt{y_2^2 + y_3^2}$ at t_0 and goes monotonically to the minima at the boundary $\psi(0) = y_3$ and $\psi(\pi) = -y_3$. Then [Equation 4.19](#) has one solution if $\frac{-\|\mathbf{y}\|^2}{2k_0} \geq -|y_3|$ and no solution otherwise. In conclusion, we have for $0 < \|\mathbf{y}\|^2 < 2k_0^2$,

$$\text{Card}(T_+^{-1}(\mathbf{y})) = \begin{cases} 2, & y_2 < 0 \text{ and } 2k_0|y_3| \leq \|\mathbf{y}\|^2 \leq 2k_0\sqrt{y_2^2 + y_3^2}, \\ 1, & y_2 < 0 \text{ and } 2k_0|y_3| > \|\mathbf{y}\|^2, \\ 1, & y_2 > 0 \text{ and } 2k_0|y_3| \geq \|\mathbf{y}\|^2, \\ 1, & y_2 = 0, \\ 0, & \text{otherwise.} \end{cases}$$

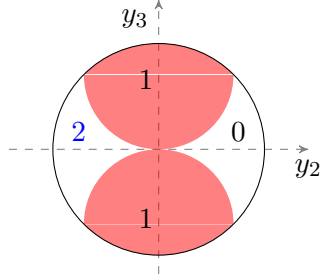


FIGURE 5. Areas of constant Banach indicatrix $\text{Card}(T^{-1}(\mathbf{y}))$ for the half rotation, sectional plot at $y_1 = 0$.

Example 4.8 (Moving rotation axis) For $c > 0$ arbitrary fixed, we consider the moving rotation axes

$$\mathbf{n}(t) = (\cos(c \sin t), \sin(c \sin t), 0)^\top,$$

and the rotation angle $\alpha(t) = t \in [0, 2\pi]$. The axes $\mathbf{n}(t)$ oscillate slightly around \mathbf{e}_1 in the r_1 - r_2 plane. Then

$$\mathbf{e}(t) = (-\sin(c \sin t) \sin t, \cos(c \sin t) \sin t, \cos t)^\top.$$

We consider $\mathbf{y} = (y_1, 0, 0)^\top \in T_+(\mathcal{U})$. Then [Proposition 4.6](#) implies that $\text{Card}(T_+^{-1}(\mathbf{y}))$ is the number of solutions t of

$$\mathbf{y} \cdot \mathbf{e}(t) = -y_1 \sin(c \sin t) \sin t = -\frac{y_1^2}{2k_0}. \quad (4.20)$$

We show that [Equation 4.20](#) has 4 solutions if $0 < y_1 < 2k_0 \sin c$. Since the function $(0, \frac{\pi}{2}) \ni t \mapsto \sin(c \sin t) \sin t$ is the composition and product of the positive, strictly increasing sine function, it is strictly increasing with supremum $\sin c$. So there is one solution $\hat{t} \in (0, \frac{\pi}{2})$ of [Equation 4.20](#). The other three solutions $\pi - \hat{t}$, $\pi + \hat{t}$, and $2\pi - \hat{t}$ follow by the symmetry of the sine. Hence, we see that $\text{Card}(T_+^{-1}(\mathbf{y})) = 4$. Since $T_+(\mathcal{U}) \ni \mathbf{y} \mapsto \mathbf{y} \cdot \mathbf{e}(t)$ is continuous, this result holds also in a small neighborhood of \mathbf{y} . However, for the point $\mathbf{y} = (0, 0, y_3)$, we see that [Equation 4.16](#) becomes

$$-y_3 \cos t = -\frac{y_3^2}{2k_0}. \quad (4.21)$$

If $0 < y_3 < 2k_0$, [Equation 4.21](#) has 2 solutions $t \in (0, 2\pi)$ and $\text{Card}(T_+^{-1}(\mathbf{y})) = 2$. By continuity, $\text{Card}(T_+^{-1}(\cdot)) = 2$ then holds in a small neighborhood of \mathbf{y} .

As T_+ maps sets of measure 0 to sets of measure 0, the considerations above show that there exist two subsets of \mathcal{U} , both of positive measure, on which $\text{Card}(T_+^{-1}(T_+(\cdot)))$ attains different values. Note that this conclusion holds for any $c > 0$ and therefore for very small movements of the rotation axis $\mathbf{n}(t)$. Taking into account the non-triviality of determining the regions of \mathcal{U} with different Banach indicatrix, this example hints to the complexity of applying the backpropagation formula [Equation 4.5](#) for general rotations.

5. DISCRETE BACKPROPAGATION AND INVERSE NDFIT

Next, we are interested in the numerical reconstruction of the three-dimensional function f from given two-dimensional functions u_t . By [Equation 4.2](#), we can build on the relation

$$-\sqrt{\frac{2}{\pi}} e^{-i\kappa r_M} \kappa i \mathcal{F}_{1,2} u_t(k_1, k_2, \pm r_M) = \mathcal{F} f(T_\pm(k_1, k_2, t)), \quad (k_1, k_2, t) \in \mathcal{U}.$$

In this paper, we work with simulated data. We assume in the numerical part that the function $\mathcal{F}f$ is known on $\mathcal{Y}_{\pm} = T_{\pm}(\mathcal{U})$. More precisely, $\mathcal{F}f$ is either given analytically or we approximate it by the computation described at the end of this section.

For $N \in 2\mathbb{N}$, let $\mathcal{I}_N := \{-\frac{N}{2} + j : j = 0, \dots, N-1\}$. We aim to reconstruct the function f with $\text{supp } f \subset \mathcal{B}_{r_s} \subset \mathbb{R}^3$ at the equispaced $N \times N \times N$ grid

$$\mathcal{R}_N := \frac{2r_s}{N} \mathcal{I}_N^3 \subset [-r_s, r_s]^3.$$

To this end, we assume that $\mathcal{F}f$ is given on the following sampling set in the k-space: let

$$\mathcal{U}_{N,S} := \left\{ (k_1, k_2, t) : (k_1, k_2) \in 2k_0 \mathcal{I}_N^2, k_1^2 + k_2^2 \leq k_0^2, t = \frac{2\pi j}{S}, j = 0, \dots, S-1 \right\}. \quad (5.1)$$

In particular, for $S := \lceil \frac{4}{\pi} N \rceil$, the number of data points $M := |\mathcal{U}_{N, \lceil \frac{4}{\pi} N \rceil}|$ is approximately equal to N^3 . In this case, we use the abbreviation $\mathcal{U}_N := \mathcal{U}_{N, \lceil \frac{4}{\pi} N \rceil}$. Then the sampling points in the k-space are given by the M points in

$$\mathcal{Y}_N^{\pm} := T_{\pm}(\mathcal{U}_N). \quad (5.2)$$

In the following, we propose two reconstruction techniques, namely the discrete backpropagation and the inverse *nonequispaced discrete Fourier transform* (NDFT). Our numerical tests will indicate that the latter appears to be preferable.

5.1. Discrete backpropagation. The discrete backpropagation is directly based on a discretization of the integral in Equation 4.6 using the values of $\mathcal{F}f$ on \mathcal{Y}_N^{\pm} . For $\mathbf{r} \in \mathcal{R}_N$, we approximate $f_{\text{bp}}(\mathbf{r})$ by

$$\mathbf{f}_{\text{bp}}(\mathbf{r}) := (2\pi)^{-\frac{3}{2}} \frac{\pi L k_0^2}{N^3} \sum_{(k_1, k_2, t) \in \mathcal{U}_N} \mathcal{F}f(T_{\pm}(k_1, k_2, t)) e^{i\mathbf{r} \cdot T_{\pm}(k_1, k_2, t)} \frac{|\nabla T_{\pm}(k_1, k_2, t)|}{\text{Card}(T_{\pm}^{-1}(T_{\pm}(k_1, k_2, t)))}. \quad (5.3)$$

We will see that evaluating \mathbf{f}_{bp} on \mathcal{R}_N is, up to the multiplicative constant in front of the sum, an adjoint NDFT applied to

$$\mathcal{F}f(T_{\pm}(k_1, k_2, t)) \frac{|\nabla T_{\pm}(k_1, k_2, t)|}{\text{Card}(T_{\pm}^{-1}(T_{\pm}(k_1, k_2, t)))}, \quad (k_1, k_2, t) \in \mathcal{U}_N.$$

Remark 5.1 For the discrete backpropagation Equation 5.3, it is crucial to know the Banach indicatrix $\text{Card}(T_{\pm}^{-1}(T_{\pm}(\cdot)))$, which we computed in some special cases, see Examples 4.4 and 4.7. However, even for a small movement of the rotation axis as in Example 4.8, it seems to be quite difficult to determine the Banach indicatrix in general. Such considerations are not necessary when applying the inverse NDFT considered next.

5.2. Inverse NDFT. To explain the inverse NDFT, we recall the NDFT first. The NDFT is the linear operator $\mathbf{F}_N : \mathbb{R}^{N^3} \rightarrow \mathbb{R}^M$ defined for our vectors $\mathbf{f}_N := (f(\mathbf{r}))_{\mathbf{r} \in \mathcal{R}_N} = (f(\frac{2r_s}{N} \mathbf{j}))_{\mathbf{j} \in \mathcal{I}_N^3}$ elementwise by

$$\mathbf{F}_N \mathbf{f}_N(\mathbf{y}) := \frac{8r_s^3}{N^3} \sum_{\mathbf{r} \in \mathcal{R}_N} f(\mathbf{r}) e^{i\mathbf{r} \cdot \mathbf{y}} = \frac{8r_s^3}{N^3} \sum_{\mathbf{j} \in \mathcal{I}_N^3} f\left(\frac{2r_s}{N} \mathbf{j}\right) e^{i\frac{2r_s}{N} \mathbf{j} \cdot \mathbf{y}}, \quad \mathbf{y} \in \mathcal{Y}_N^{\pm}, \quad (5.4)$$

see [38, Section 7.1]. In other words, we can consider the NDFT via the tensor $\mathbf{F}_N = \left(e^{i\frac{2r_s}{N}\mathbf{j}\cdot\mathbf{y}} \right)_{\mathbf{j}\in\mathcal{I}_N^3, \mathbf{y}\in\mathcal{Y}_N^\pm}$. Furthermore, it provides an approximation of the Fourier transform

$$\mathcal{F}f(\mathbf{y}) \approx \mathbf{F}_N \mathbf{f}_N(\mathbf{y}), \quad \mathbf{y} \in \mathcal{Y}_N^\pm.$$

Then, as already mentioned above, the discrete backpropagation formula Equation 5.3 is just the application of the adjoint NDFT to weighted values $(\mathcal{F}f(\mathbf{y}))_{\mathbf{y}\in\mathcal{Y}_N^\pm}$. In contrast, the inverse NDFT reconstructs the values $(f(\mathbf{r}))_{\mathbf{r}\in\mathcal{R}_N}$ by solving the least squares problem

$$\operatorname{argmin}_{\mathbf{f}\in\mathbb{R}^{N^3}} \|\mathbf{F}_N \mathbf{f} - (\mathcal{F}f(\mathbf{y}))_{\mathbf{y}\in\mathcal{Y}_N^\pm}\|_2^2. \quad (5.5)$$

More precisely, we call a solution of this problem *inverse NDFT* of $(\mathcal{F}f(\mathbf{y}))_{\mathbf{y}\in\mathcal{Y}_N^\pm}$, see [38, Section 7.6.2].

Remark 5.2 (Fast Computation by NFFT) Computationally we will solve the least squares problem Equation 5.5 by a *conjugate gradient method on the normal equations* (CGNE) as proposed in [31]. Each iteration step of the CGNE algorithm requires the computation of an NDFT and an adjoint NDFT. Both the computation of the NDFT and its adjoint can be realized in an efficient way by the so-called *nonequispaced fast Fourier transform* (NFFT). The NFFT requires only $\mathcal{O}(N^3 \log N)$ arithmetic operations instead of $\mathcal{O}(N^6)$ operations for the NDFT and is highly recommendable in 3D. Depending on the choice of the inner parameters, the NFFT provides an arbitrarily tight approximation of the NDFT, see, e.g., [4, 14, 42].

Computation of k-space data. If the function $\mathcal{F}f$ or its values at \mathcal{Y}_N^\pm are not given, we have to synthesize them for our numerical tests. Since the function f is known in our synthetic examples and can therefore be sampled on an arbitrary fine grid, we choose $n \gg N$ and approximate the values $\mathcal{F}f(\mathbf{y})$ by applying the NDFT on the fine grid, i.e., we take

$$\mathcal{F}f(\mathbf{y}) \approx \frac{8r_s^3}{n^3} \sum_{\mathbf{r}\in\mathcal{R}_n} f(\mathbf{r}) e^{i\mathbf{r}\cdot\mathbf{y}} = \frac{8r_s^3}{n^3} \sum_{\mathbf{j}\in\mathcal{I}_n^3} f\left(\frac{2r_s}{n}\mathbf{j}\right) e^{i\frac{2r_s}{n}\mathbf{j}\cdot\mathbf{y}}, \quad \mathbf{y} \in \mathcal{Y}_N \quad (5.6)$$

as given values for both the discrete backpropagation and the inverse NDFT. We note that Equation 5.6 resembles \mathbf{F}_n evaluated on a different grid than in Equation 5.4.

6. NUMERICAL TESTS

In this section, we demonstrate the performance of the discrete backpropagation in Equation 5.3 and the inverse NDFT defined in Equation 5.5 by numerical examples. For computing the NDFT and its adjoint, we apply the NFFT software library [29]. If not stated otherwise, we use the NFFT for all reconstructions. We fixed the number of CGNE iteration steps in the inverse NDFT to 20. In this section, we concentrate on the transmission imaging associated with T_+ .

6.1. Sampling. The wavelength λ is related with the wave number via $k_0 = \frac{2\pi}{\lambda}$. Since the discretized Fourier transform $\mathbf{F}_N f(\mathbf{y})$ is $\frac{\pi N}{r_s}$ -periodic in \mathbf{y} and the data points $\mathbf{y} \in \mathcal{Y}_N^+$ satisfy $\|\mathbf{y}\| \leq \sqrt{2}k_0$, it is reasonable that the model parameters satisfy $\sqrt{2}k_0 \leq \frac{\pi N}{2r_s}$ or, equivalently,

$$N \geq \frac{2\sqrt{2}k_0 r_s}{\pi} = \frac{4\sqrt{2}r_s}{\lambda}.$$

In particular, we choose $N = \frac{2\sqrt{2}k_0 r_s}{\pi}$, where we note that r_s can always be made larger in order to make sure that N is an integer. The distance between adjacent grid points $\mathbf{r} \in \mathcal{R}_N$ is then

N	80	160	240	320	400	800
RMSE	3.72 E-2	9.37 E-3	4.38 E-3	2.58 E-3	1.67 E-3	4.46 E-4

TABLE 1. The root mean square error (RMSE) of $\mathbf{F}_N f_a$ with respect to $\mathcal{F}f_a$ in dependence on the grid size N for the NDFT.

$\frac{2r_s}{N} = \frac{\lambda}{2\sqrt{2}}$, which only depends on the wavelength λ . In our numerical tests, we fix the wavelength $\lambda = 1$ such that all measurements in \mathbf{r} are in multiples of the wavelength. Hence, the wave number is $k_0 = 2\pi$. The data points $T_+(k_1, k_2, t)$ in the k-space are on the grid \mathcal{Y}_N^+ described in the Equation 5.2. Therefore all data points in \mathcal{Y}_N^+ are contained in a ball of radius $\sqrt{2}k_0 \approx 8.89$.

In our first numerical tests, we choose the grid size $N = 80$ which corresponds to the radius $r_s = \frac{\lambda N}{4\sqrt{2}} \approx 14.1\lambda$ of the maximal support of f . Then we have $N^3 = 512\,000$ grid points in \mathcal{R}_N and 496 944 data points in \mathcal{Y}_N^+ . If not available analytically, we simulated the values $\mathcal{F}f(\mathbf{y})$, $\mathbf{y} \in \mathcal{Y}_N^+$, by an NDFT of length $n = 5N$ as in Equation 5.6.

We compare the reconstruction quality based on the the *structural similarity index measure* (SSIM) [48] and the *peak signal-to-noise ratio* (PSNR) determined by

$$\text{PSNR}(\mathbf{f}, \mathbf{g}) := 10 \log_{10} \frac{\max_{\mathbf{r} \in \mathcal{R}_N} |\mathbf{f}(\mathbf{r})|^2}{N^{-3} \sum_{\mathbf{r} \in \mathcal{R}_N} |\mathbf{f}(\mathbf{r}) - \mathbf{g}(\mathbf{r})|^2},$$

where \mathbf{f} is the ground truth and \mathbf{g} is the reconstructed value. Note that higher values indicate a better reconstruction quality for both. If $\mathcal{F}f(\mathbf{y})$, $\mathbf{y} \in \mathcal{Y}_N^+$ is computed from the function values at a fine grid, then it appears reasonable to take as ground truth for the PSNR the voxel values which are the averages of their five-point neighborhood on the fine grid

$$\mathbf{f}_N^{\text{av}}(\mathbf{r}) := \frac{1}{5^3} \sum_{\mathbf{j} \in \{-2, -1, \dots, 2\}^3} f\left(\mathbf{r} + \frac{2r_s}{5N}\mathbf{j}\right), \quad \mathbf{r} \in \mathcal{R}_N.$$

6.2. Function with exactly known Fourier transform. In order to illustrate the effectiveness of the proposed reconstruction algorithms, we make the first test with the characteristic function $f_a(\mathbf{r}) = \mathbf{1}_{B_a}(\mathbf{r})$ of the ball with radius $a > 0$. Its Fourier transform is known analytically,

$$\mathcal{F}f_a(\mathbf{y}) = \sqrt{\frac{2}{\pi}} \frac{1}{\|\mathbf{y}\|^3} (\sin \|a\mathbf{y}\| - \|a\mathbf{y}\| \cos \|a\mathbf{y}\|), \quad \mathbf{y} \in \mathbb{R}^3, \quad (6.1)$$

see [38, p. 183]. The object is fully rotated around the axis $\mathbf{n}(t) = \mathbf{e}_1$ and angle $\alpha(t) = t$, $t \in [0, 2\pi]$, as in Example 4.4. We consider the two cases that the input for our reconstruction arises from i) the exact data $\mathcal{F}f_a(\mathbf{y})$ by Equation 6.1, and ii) the approximate data $\mathbf{F}_{5N}f_a$ by Equation 5.6. The error between the approximation $\mathbf{F}_N f_a(\mathbf{y})$ and the true values $\mathcal{F}f_a(\mathbf{y})$, $\mathbf{y} \in \mathcal{Y}_N^+$, is shown for different N in Table 1.

The reconstruction is depicted in Figure 6. For both cases, we compare the inverse NDFT with the discrete backpropagation Equation 5.3. The latter shows stronger artifacts due to the sharp cutoff in the k-space. There is almost no difference between the exact data in i) and approximate ones in ii); since the approximate data is computed on a very fine grid.

6.3. Simple test function. As a second test function f , we take the characteristic function of a ball and cut out a small segment around the plane $\{r_2 = 0\}$. The rotation is around the r_1

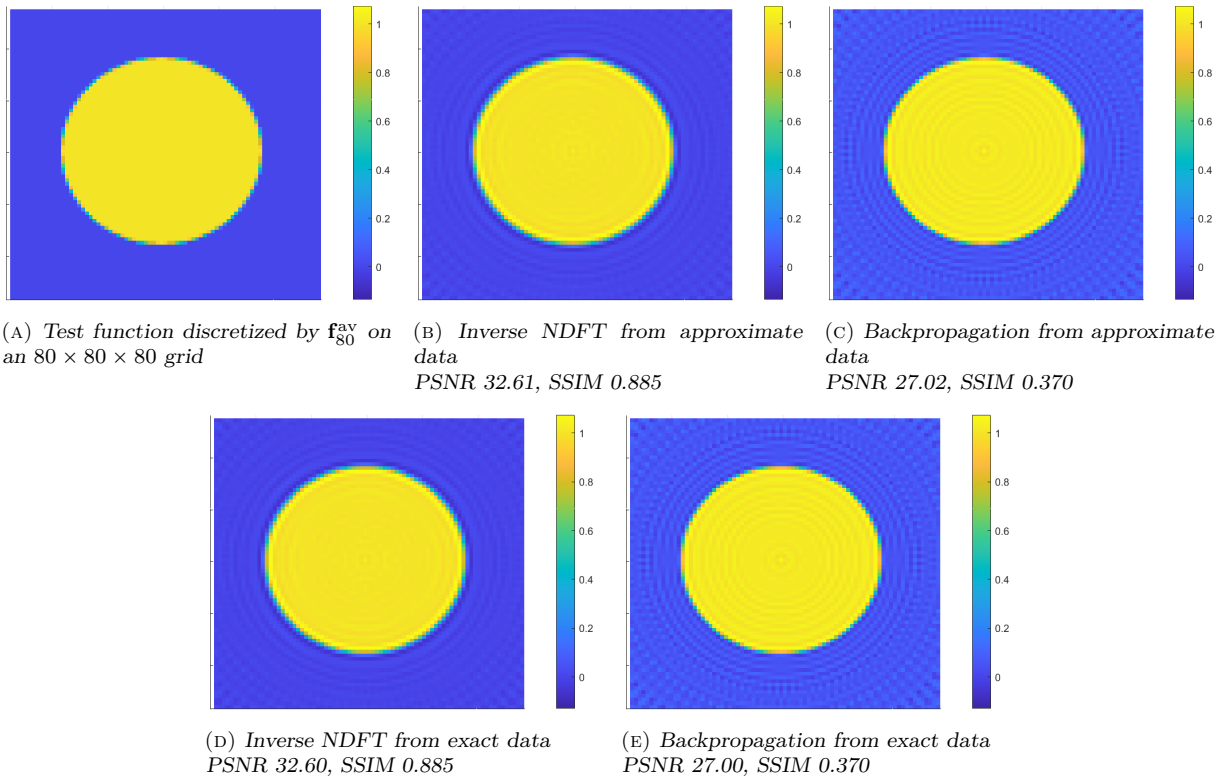


FIGURE 6. Test with the characteristic function f_a of a ball of radius $a = 9$, with resolution $N = 80$. All plots show the slice of the 3D function at $r_1 = -0.3$. The reconstructions use either the exact data $\mathcal{F}f_a$, or the approximated data from Equation 5.6. In both cases, we use the same set of points \mathcal{Y}_N^+ .

axis as in the previous test. The reconstruction results are shown in Figure 7, where the inverse NDFT yields an image with fewer artifacts than the discrete backpropagation.

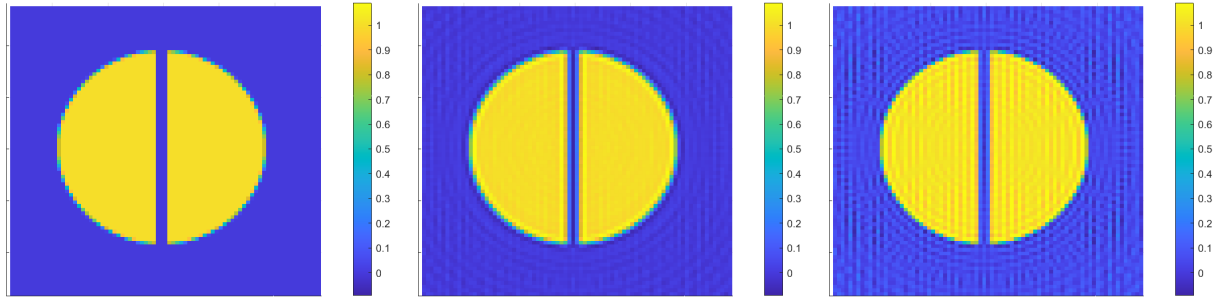
The reconstruction becomes more difficult when the object has discontinuities perpendicular to the rotation axis. To this end, we take the previous test function, but the rotation is now around the r_2 axis. The reconstruction in Figure 8 resolves the gap considerably worse than in the previous example. This is because we do not have any data of the Fourier transform $\mathcal{F}f$ near the k_2 axis away from the origin. However, the information about the Fourier transform in this region is important due to the singularities of f along planes perpendicular to the r_2 axis. Again, the discrete backpropagation produces more artifacts than the inverse NDFT.

6.4. Perturbed rotation. In practical applications, the rotation of the object is often a little perturbed. For the following test, we consider the rotation angle $\alpha(t) = t$ and the slightly moving rotation axis

$$\mathbf{n}(t) = \left(\cos\left(\frac{\pi}{8} \sin t\right), \sin\left(\frac{\pi}{8} \sin t\right), 0 \right)^\top,$$

see Example 4.8. This axis $\mathbf{n}(t)$ is in the $r_1 r_2$ plane and it moves around \mathbf{e}_1 . The reconstruction results are depicted in Figure 9, where we chose the resolution $N = 160$ and thus $r_s \approx 28.3$. In these tests, the perturbation slightly improves the quality of the reconstructions, because the set of missing k-space data is different. We note that we applied the discrete backpropagation Equation 5.3 with Banach indicatrix $\text{Card}(T_+^{-1}) \equiv 2$, even though it is 4 in a small region. This still results in a good approximation.

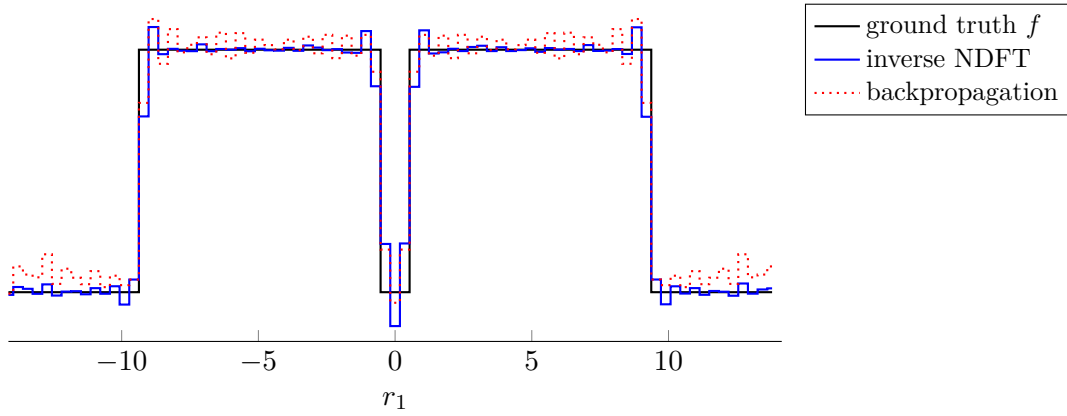
In case of a half rotation around the fixed axis \mathbf{e}_1 , we have an explicit formula of the Banach



(A) Test function (ground truth image) on an $80 \times 80 \times 80$ grid

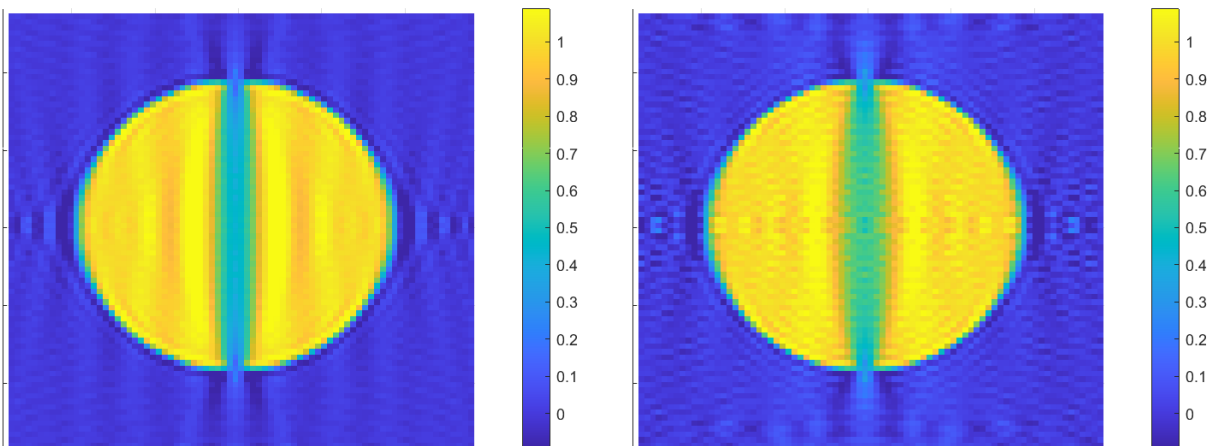
(B) Inverse NDFT reconstruction PSNR 29.52, SSIM 0.863

(C) Backpropagation PSNR 25.25, SSIM 0.366



(D) Comparison of both reconstructions and the ground truth at the line $(r_1, 0, 0)^T$

FIGURE 7. Top: Slice plot of the test function with discontinuity around the plane $r_2 = 0$, and its reconstructions. Bottom: Sectional plot of test function and its reconstructions.



(A) Inverse NDFT reconstruction PSNR 22.94, SSIM 0.658

(B) Backpropagation PSNR 21.04, SSIM 0.341

FIGURE 8. The same setting and test function as in Figure 7, but this time the object is rotated around \mathbf{e}_2 instead of \mathbf{e}_1 .

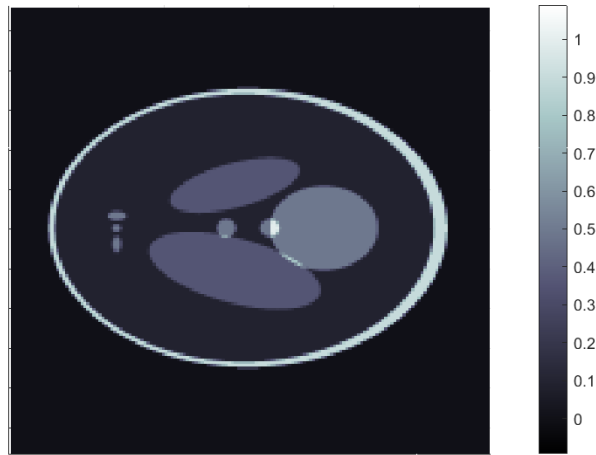
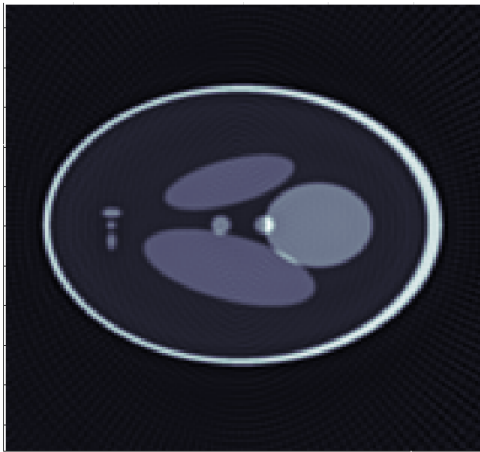
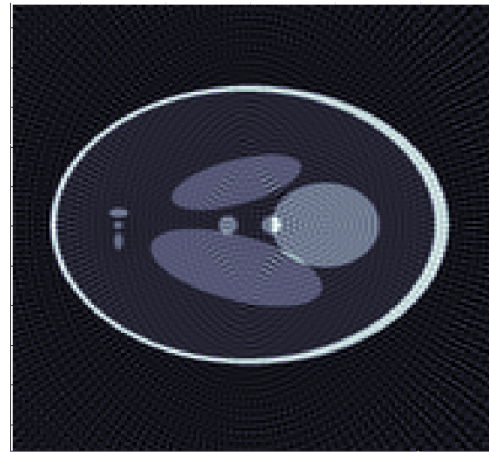
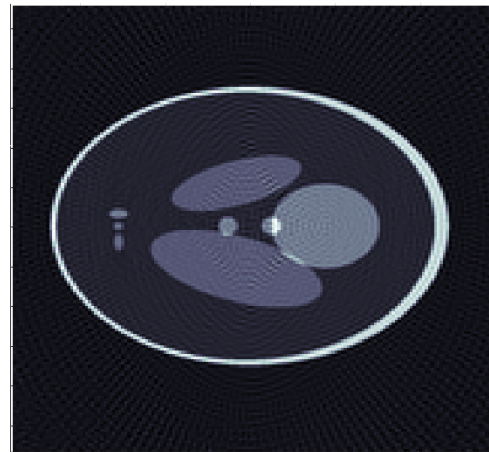
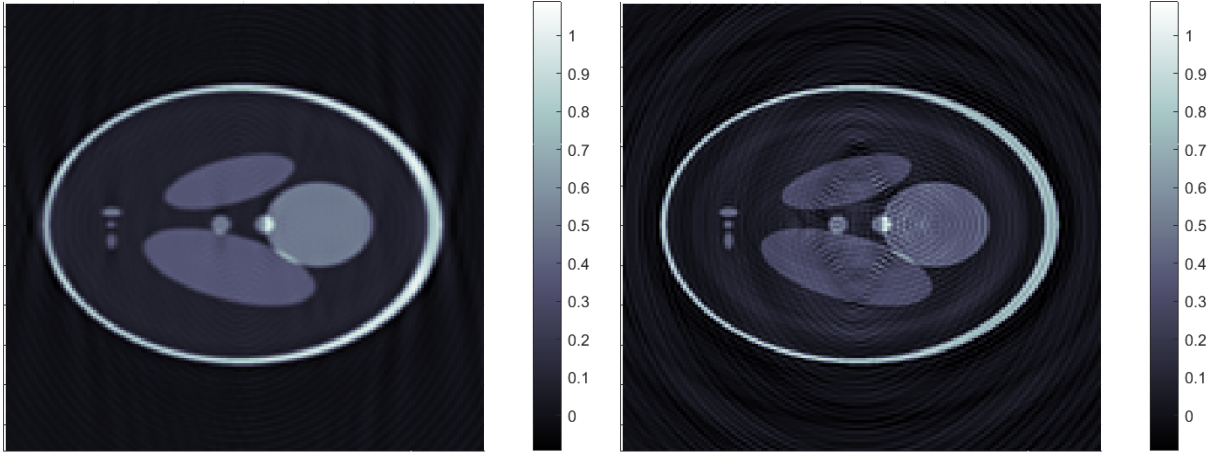
(A) Phantom f_{160}^{av} on a $160 \times 160 \times 160$ grid(B) Inverse NDFT reconstruction with fixed rotation axis
PSNR 32.56, SSIM 0.892(C) Backpropagation with fixed rotation axis
PSNR 27.81, SSIM 0.422(D) Inverse NDFT reconstruction with slightly moving axis
PSNR 33.62, SSIM 0.934(E) Backpropagation with slightly moving axis
PSNR 30.92, SSIM 0.549

FIGURE 9. A Shepp–Logan phantom as test function (A) with the bigger resolution $N = 160$. Reconstruction for the constant rotation axis $\mathbf{n}(t) = \mathbf{e}_1$ with the inverse NDFT (B) and with the backpropagation (C). With the slightly moving rotation axis $\mathbf{n}(t)$, the inverse NDFT (D) again produces a clearer image than the backpropagation (E).



(A) Inverse NDFT
PSNR 30.80, SSIM 0.816

(B) Backpropagation
PSNR 26.01, SSIM 0.324

FIGURE 10. Reconstruction for a half rotation around \mathbf{e}_1 , all other parameters are the same as in Figure 9.

indicatrix, see Example 4.7. The reconstruction shown in Figure 10 behaves slightly worse than before, due to the missing data.

Remark 6.1 (Computation time) The discrete backpropagation in Equation 5.3 consists of one adjoint NDFT, whereas each iteration step of the CGNE method of the inverse NDFT requires about twice the computational effort: to perform both an NDFT and an adjoint NDFT. Hence, the backpropagation algorithm is considerably faster than the inverse NDFT. In practice, this difference is a little smaller, since the NFFT software includes a node-dependent precomputation, which has to be done only once. For the grid size of $N = 160$, which corresponds to approximately 4 million grid points, the discrete backpropagation takes about 9.6 seconds, whereas 20 iteration steps of the CGNE algorithm take 46 seconds on an Intel Core i7-10700 CPU.

6.5. Noisy measurements. In practical applications, the measurements are corrupted by noise. For some noise level $\delta > 0$, we consider the Gaussian white noise model

$$\mathbf{g}^\delta(\mathbf{y}) := \mathcal{F}f(\mathbf{y}) + \delta \mathcal{N}(0, 1), \quad \mathbf{y} \in \mathcal{Y}_N^+.$$

The CGNE method used for the inverse NDFT is a regularizer with the number of iterations as the regularization parameter. Let us denote by \mathbf{f}_k^δ the k -th iterate of the CGNE method applied to \mathbf{g}^δ . The discrepancy principle [16, Section 7.3] states to choose k such that the residual $\|\mathbf{F}_N \mathbf{f}_k^\delta - \mathbf{g}^\delta\|$ is approximately δ . A popular parameter choice rule requiring no knowledge of the noise level δ is the L-curve method [23], where one chooses k at the corner in the log-log plot of the residual $\|\mathbf{F}_N \mathbf{f}_k^\delta - \mathbf{g}^\delta\|$ versus the norm of the approximate solution $\|\mathbf{f}_k^\delta\|$. As discrete norm, we take the root mean square

$$\|\mathbf{g}^\delta\| := \left(\frac{1}{|\mathcal{Y}_N^+|} \sum_{\mathbf{y} \in \mathcal{Y}_N^+} |\mathbf{g}^\delta(\mathbf{y})|^2 \right)^{1/2}.$$

For an overview of parameter choice rules in the conjugate gradient method, we refer to [22].

In Table 2, we show the reconstruction error with different parameter choice rules. We use the same test function as in Figure 9, the resolution $N = 160$, and the rotation around the r_1 axis. We compute the corner of the L-curve according to [24]. The L-curve method tends to overestimate the stopping index k , whereas the discrepancy principle produces slightly better reconstructions.

Noise level $\frac{\delta}{\max \mathcal{F}f }$	Best choice	L-curve	Discrepancy	Backpropagation
0.0 %	33.01 (100)	–	–	27.81
0.1 %	30.98 (18)	27.80 (65)	30.16 (13)	23.25
0.2 %	28.84 (13)	25.89 (29)	28.07 (10)	18.49
0.5 %	25.20 (8)	18.81 (25)	24.07 (6)	11.04
1.0 %	22.58 (6)	20.78 (3)	20.78 (3)	5.03

TABLE 2. PSNR for with different noise levels δ with the L-curve method and discrepancy principle for choosing the number k of CGNE iteration, which is displayed in parantheses. The best choice serves as a benchmark; it is attained at the iteration index k which maximizes $\text{PSNR}(\mathbf{f}^{\text{av}}, \mathbf{f}_k^{\delta})$ among $k = 1, \dots, 100$, where we know the ground truth \mathbf{f}^{av} . The backpropagation contains no regularization and thus works only well with very small noise. The function f is the same as in Figure 9 with constant rotation axis \mathbf{e}_1 and resolution $N = 160$.

7. APPENDIX

7.1. Distributions and the Fourier Transform. This section collects several results about distributions and the Fourier transform. We refer to [20, 26, 38, 39] for more details.

Definition 7.1 (Test function) The space $\mathcal{D}(\mathbb{R}^n)$ of test functions is the set of all infinitely differentiable functions $\phi : \mathbb{R}^n \rightarrow \mathbb{C}$ with compact support equipped with the inductive limit topology.

Definition 7.2 (Distribution) The space $\mathcal{D}'(\mathbb{R}^n)$ of distributions is the topological dual of $\mathcal{D}(\mathbb{R}^n)$, i.e. the space of all functionals $v : \mathcal{D}(\mathbb{R}^n) \rightarrow \mathbb{C}$ such that

$$v[a\phi + b\psi] = av[\phi] + bv[\psi]$$

for all $a, b \in \mathbb{C}$ and $\phi, \psi \in \mathcal{D}(\mathbb{R}^n)$ and

$$v[\phi_n] \rightarrow v[\phi]$$

whenever $\phi_n \rightarrow \phi$ in $\mathcal{D}(\mathbb{R}^n)$.

Example 7.3 Every locally absolutely integrable function $v \in L^1_{\text{loc}}(\mathbb{R}^n)$ can be identified with a distribution via

$$\phi \mapsto \int_{\mathbb{R}^n} v(\mathbf{r})\phi(\mathbf{r}) \, d\mathbf{r}.$$

It is common to use the same symbol for the function and the associated distribution.

By $L^p(\Omega)$, $p \in [1, \infty]$, we denote the Banach space of (equivalence classes of) complex-valued functions with finite norm

$$\|f\|_{L^p} := \left(\int_{\Omega} |f(\mathbf{r})|^p \, d\mathbf{r} \right)^{\frac{1}{p}}, \quad p \in [1, \infty),$$

$$\|f\|_{L^\infty} := \text{esssup}_{\mathbf{r} \in \Omega} |f(\mathbf{r})|.$$

If $\Omega \subset \mathbb{R}^n$ is bounded, then these spaces are continuously embedded, i.e., for $1 \leq p \leq q$, we have

$$L^q(\Omega) \hookrightarrow L^p(\Omega). \tag{7.1}$$

The functions of $\mathcal{D}(\mathbb{R}^n)$ form a dense set in $L^p(\mathbb{R}^n)$, $p \in [1, \infty)$.

Definition 7.4 (Fourier transform on $L^1(\mathbb{R}^n)$) The Fourier transform of a function $g \in L^1(\mathbb{R}^n)$ is defined by

$$\mathcal{F}g(\mathbf{k}) := (2\pi)^{-\frac{n}{2}} \int_{\mathbb{R}^n} g(\mathbf{r})e^{-i\mathbf{k}\cdot\mathbf{r}} d\mathbf{r} \quad (7.2)$$

for all $\mathbf{k} \in \mathbb{R}^n$.

The Fourier transform $\mathcal{F} : L^1(\mathbb{R}^n) \rightarrow C_0(\mathbb{R}^n)$ is a linear, continuous operator into the space $C_0(\mathbb{R}^n)$ of continuous functions vanishing at infinity with operator norm $\|\mathcal{F}\|_{L^1 \rightarrow C_0} = (2\pi)^{-\frac{n}{2}}$. In contrast, the Fourier transform on the two spaces introduced next, maps again onto the same space.

Definition 7.5 (Schwartz space) The Schwartz space $S(\mathbb{R}^n)$ consists of all infinitely differentiable functions $\phi : \mathbb{R}^n \rightarrow \mathbb{C}$ such that

$$p_{\alpha,\beta}(\phi) := \sup_{\mathbf{r} \in \mathbb{R}^n} |\mathbf{r}^\alpha \partial^\beta \phi(\mathbf{r})| < +\infty$$

for all multi-indices $\alpha, \beta \in \mathbb{N}_0^n$. The topology on $S(\mathbb{R}^n)$ is induced by the seminorms $p_{\alpha,\beta}$.

Definition 7.6 (Tempered distribution) The space $S'(\mathbb{R}^n)$ of tempered distributions is the topological dual of $S(\mathbb{R}^n)$.

Example 7.7 Every function $v \in L^1_{\text{loc}}(\mathbb{R}^n)$ that is polynomially bounded for $\|\mathbf{r}\| \rightarrow \infty$ can be identified with a tempered distribution via

$$\phi \mapsto \int_{\mathbb{R}^n} v(\mathbf{r})\phi(\mathbf{r}) d\mathbf{r}.$$

For the following result note that $S(\mathbb{R}^n) \subset L^1(\mathbb{R}^n)$.

Proposition 7.8 *The Fourier transform is a linear, bijective, continuous operator $\mathcal{F} : S(\mathbb{R}^n) \rightarrow S(\mathbb{R}^n)$. It has a continuous inverse defined by*

$$\mathcal{F}^{-1}\phi(\mathbf{r}) := (2\pi)^{-\frac{n}{2}} \int_{\mathbb{R}^n} \phi(\mathbf{k})e^{i\mathbf{k}\cdot\mathbf{r}} d\mathbf{k}$$

for all $\phi \in S(\mathbb{R}^n)$ and $\mathbf{r} \in \mathbb{R}^n$.

Observe that

$$\int_{\mathbb{R}^n} \phi(\mathbf{r}) \mathcal{F}\psi(\mathbf{r}) d\mathbf{r} = \int_{\mathbb{R}^n} \mathcal{F}\phi(\mathbf{r}) \psi(\mathbf{r}) d\mathbf{r}, \quad (7.3)$$

holds for all $\phi, \psi \in S(\mathbb{R}^n)$. Combined with the fact that, for every $v \in S'(\mathbb{R}^n)$, the map $\phi \mapsto v[\mathcal{F}\phi]$ is another tempered distribution we are led to the following extension of the Fourier transform.

Definition 7.9 (Fourier transform on $S'(\mathbb{R}^n)$) The Fourier transform of $v \in S'(\mathbb{R}^n)$ is defined by

$$\mathcal{F}v[\phi] := v[\mathcal{F}\phi]$$

for all $\phi \in S(\mathbb{R}^n)$.

With this definition, [Proposition 7.8](#) carries over to $S'(\mathbb{R}^n)$.

Proposition 7.10 *The Fourier transform is a linear, bijective, continuous operator $\mathcal{F} : S'(\mathbb{R}^n) \rightarrow S'(\mathbb{R}^n)$. It has a continuous inverse defined by*

$$\mathcal{F}^{-1}v[\phi] = v[\mathcal{F}^{-1}\phi]$$

for all $v \in S'(\mathbb{R}^n)$ and $\phi \in S(\mathbb{R}^n)$.

Remark 7.11 Many other operations can be extended from $S(\mathbb{R}^n)$ to $S'(\mathbb{R}^n)$ in a way similar to [Definition 7.9](#). Suppose $A : S(\mathbb{R}^n) \rightarrow S(\mathbb{R}^n)$ is linear and bounded, and that there is another linear, bounded operator $B : S(\mathbb{R}^n) \rightarrow S(\mathbb{R}^n)$ such that $\int_{\mathbb{R}^n} (A\phi)\psi = \int_{\mathbb{R}^n} \phi(B\psi)$ for all Schwartz functions ϕ and ψ . Then A can be uniquely extended to $S'(\mathbb{R}^n)$ by setting $Au[\phi] = u[B\phi]$. See [\[20, Rem. 5.15\]](#) for more details.

Two further operations which can be extended from $S(\mathbb{R}^n)$ to $S'(\mathbb{R}^n)$ in the way explained above are multiplication and convolution with a Schwartz function. Both $\phi \mapsto \psi\phi$ and $\phi \mapsto \psi * \phi$ map $S(\mathbb{R}^n)$ continuously into itself. Moreover, regarding convolution note that we have

$$\int_{\mathbb{R}^n} (\psi * \eta)(\mathbf{r})\phi(\mathbf{r}) d\mathbf{r} = \int_{\mathbb{R}^n} \eta(\mathbf{r})(M\psi * \phi)(\mathbf{r}) d\mathbf{r} \quad (7.4)$$

for all $\phi, \psi, \eta \in S(\mathbb{R}^n)$, where the operator $M : S(\mathbb{R}^n) \rightarrow S(\mathbb{R}^n)$ is given by $M\phi(x) = \phi(-x)$. This gives rise to the following definition.

Definition 7.12 (Convolution of a Schwartz function with a tempered distribution)

The convolution of $\psi \in S(\mathbb{R}^n)$ with $v \in S'(\mathbb{R}^n)$ is defined by

$$(\psi * v)[\phi] := v[M\psi * \phi]$$

for all $\phi \in S(\mathbb{R}^n)$.

The following result relates the operations of multiplication and convolution by means of the Fourier transform.

Theorem 7.13 (Convolution Theorem) *For all $\phi \in S(\mathbb{R}^n)$ and all $v \in S'(\mathbb{R}^n)$, we have*

$$\mathcal{F}(\phi * v) = (2\pi)^{\frac{n}{2}} \mathcal{F}\phi \mathcal{F}v \quad \text{and} \quad \mathcal{F}\phi * \mathcal{F}v = (2\pi)^{\frac{n}{2}} \mathcal{F}(\phi v).$$

Note that [Theorem 7.13](#) remains true, if we replace \mathcal{F} by \mathcal{F}^{-1} .

7.2. Partial Fourier transforms. In the following, we introduce partial Fourier transforms, and show that they are well-defined on $S'(\mathbb{R}^n)$. In other words, we prove that an m -dimensional Fourier transform ($m < n$) is well-defined for n -dimensional tempered distributions and that it possesses an appropriate convolution property.

Definition 7.14 (Partial Fourier transforms on $S(\mathbb{R}^n)$) For $j \in \{1, \dots, n\}$, we define the partial Fourier transform \mathcal{F}_j of $\phi \in S(\mathbb{R}^n)$ by

$$\mathcal{F}_j\phi(r_1, \dots, r_{j-1}, k_j, r_{j+1}, \dots, r_n) = (2\pi)^{-\frac{1}{2}} \int_{\mathbb{R}} \phi(r_1, \dots, r_{j-1}, s, r_{j+1}, \dots, r_n) e^{-ik_j s} ds. \quad (7.5)$$

More generally, for an index set $I = \{j_1, \dots, j_m\} \subset \{1, \dots, n\}$, the partial Fourier transform $\mathcal{F}_I\phi$ of $\phi \in S(\mathbb{R}^n)$ is defined by

$$\mathcal{F}_I\phi := \mathcal{F}_{j_m} \cdots \mathcal{F}_{j_1}\phi. \quad (7.6)$$

Note that, for fixed $r_1, \dots, r_{j-1}, r_{j+1}, \dots, r_n$, the map $r_j \mapsto \phi(\mathbf{r})$, defines a Schwartz function on \mathbb{R} . This function is then also in $L^1(\mathbb{R})$ and therefore the integral in Equation 7.5 is well-defined. Moreover, by the Fubini-Tonelli theorem the order in which the \mathcal{F}_i appear in Equation 7.6 does not matter. Finally, we point out that $\mathcal{F}_{1, \dots, n} = \mathcal{F}$.

Proposition 7.15 *Partial Fourier transforms are linear, bijective, continuous operators $\mathcal{F}_I : S(\mathbb{R}^n) \rightarrow S(\mathbb{R}^n)$. They have continuous inverses defined by*

$$\mathcal{F}_I^{-1}\phi := \mathcal{F}_{j_m}^{-1} \dots \mathcal{F}_{j_1}^{-1}\phi,$$

where

$$\mathcal{F}_j^{-1}\phi(r_1, \dots, r_{j-1}, k_j, r_{j+1}, \dots, r_n) = (2\pi)^{-\frac{1}{2}} \int_{\mathbb{R}} \phi(r_1, \dots, r_{j-1}, s, r_{j+1}, \dots, r_n) e^{ik_j s} ds.$$

Proof: This result can be shown in essentially the same way as Proposition 7.8. The main steps are as follows.

First, from Equation 7.5 and Equation 7.6 we deduce that the function $\mathcal{F}_I\phi$ is bounded. Second, it is infinitely differentiable and the operator \mathcal{F}_I exchanges differentiation and multiplication with polynomials in the expected way. More specifically, and assuming that $I = \{1, \dots, m\}$ to keep the notation simple, we have

$$(\mathbf{k}, \mathbf{r})^\alpha \partial^\beta \mathcal{F}_I\phi = (-i)^{|\alpha_1| + |\beta_1|} \mathcal{F}_I \left(\partial_{\mathbf{s}}^{\alpha_1} \mathbf{r}^{\alpha_2} \mathbf{s}^{\beta_1} \partial_{\mathbf{r}}^{\beta_2} \phi \right) \quad (7.7)$$

for all $\mathbf{k} \in \mathbb{R}^m$, $\mathbf{r} \in \mathbb{R}^{n-m}$ and all multi-indices $\alpha = (\alpha_1, \alpha_2), \beta = (\beta_1, \beta_2) \in \mathbb{N}_0^m \times \mathbb{N}_0^{n-m}$. These two facts imply that $\mathcal{F}_I\phi \in S(\mathbb{R}^n)$.

Next, exploiting Equation 7.7, we can show that for each pair of multi-indices α, β there exists another pair α', β' and a $C > 0$ such that $p_{\alpha, \beta}(\mathcal{F}_I\phi) \leq Cp_{\alpha', \beta'}(\phi)$. This shows that \mathcal{F}_I is continuous on $S(\mathbb{R}^n)$.

Finally, note that $\mathbf{k} \mapsto \mathcal{F}_I\phi(\mathbf{k}, \mathbf{r})$ is nothing but the regular Fourier transform of the Schwartz function $\mathbf{s} \mapsto \phi(\mathbf{s}, \mathbf{r})$. Therefore \mathcal{F}_I has an inverse. It is continuous on $S(\mathbb{R}^n)$ for the same reasons \mathcal{F}_I is. \square

Since Equation 7.3 remains valid if we replace \mathcal{F} by \mathcal{F}_I , we can extend the partial Fourier transforms to $S'(\mathbb{R}^n)$.

Definition 7.16 (Partial Fourier transforms on $S'(\mathbb{R}^n)$) For every $v \in S'(\mathbb{R}^n)$, we define $\mathcal{F}_I v$ by

$$\mathcal{F}_I v[\phi] := v[\mathcal{F}_I\phi]$$

for all $\phi \in S(\mathbb{R}^n)$.

Proposition 7.17 *Partial Fourier transforms are linear, bijective, continuous operators $\mathcal{F}_I : S'(\mathbb{R}^n) \rightarrow S'(\mathbb{R}^n)$. They have continuous inverses defined by*

$$\mathcal{F}_I^{-1}v[\phi] = v[\mathcal{F}_I^{-1}\phi]$$

for all $v \in S'(\mathbb{R}^n)$ and all $\phi \in S(\mathbb{R}^n)$.

Proof: The continuity of the extension of \mathcal{F}_I to $S'(\mathbb{R}^n)$ follows from Remark 7.11. Analogously, \mathcal{F}_I^{-1} can be extended to a continuous operator on $S'(\mathbb{R}^n)$. These two extensions are still inverse to each other, because $\mathcal{F}_I \mathcal{F}_I^{-1}v[\phi] = v[\mathcal{F}_I^{-1} \mathcal{F}_I\phi] = v[\phi] = \mathcal{F}_I^{-1} \mathcal{F}_I v[\phi]$. \square

Remark 7.18 It follows from [Definition 7.14](#) that partial Fourier transforms can be composed in the following way. Suppose I and J are disjoint subsets of $\{1, \dots, n\}$. Then an application of the Fubini-Tonelli theorem shows that $\mathcal{F}_I \mathcal{F}_J \phi = \mathcal{F}_{I \cup J} \phi$ for every $\phi \in S(\mathbb{R}^n)$. This property immediately carries over to the distributional setting

$$\mathcal{F}_I \mathcal{F}_J v[\phi] = v[\mathcal{F}_J \mathcal{F}_I \phi] = v[\mathcal{F}_{I \cup J} \phi] = \mathcal{F}_{I \cup J} v[\phi]$$

for all $v \in S'(\mathbb{R}^n)$ and all $\phi \in S(\mathbb{R}^n)$. In the proof of [Theorem 3.1](#), where $n = 3$, we make use of the special case $\mathcal{F}_3 \mathcal{F}_{1,2} = \mathcal{F}$ implying that

$$\mathcal{F}_{1,2} = \mathcal{F}_3^{-1} \mathcal{F}. \quad (7.8)$$

Definition 7.19 (Partial convolution on $S(\mathbb{R}^n)$) Let $j \in \{1, \dots, n\}$ and $\phi, \psi \in S(\mathbb{R}^n)$. We denote by $\phi \overset{j}{*} \psi$ the convolution of ϕ and ψ along the j -th coordinate, i.e.,

$$(\phi \overset{j}{*} \psi)(\mathbf{r}) := \int_{\mathbb{R}} \phi(r_1, \dots, r_{j-1}, s, r_{j+1}, \dots, r_n) \psi(r_1, \dots, r_{j-1}, r_j - s, r_{j+1}, \dots, r_n) ds.$$

As is the case for ordinary convolution, partial convolution with a Schwartz function is a continuous operation on $S(\mathbb{R}^n)$.

Proposition 7.20 For every $\psi \in S(\mathbb{R}^n)$ and $j \in \{1, \dots, n\}$ the operation $\phi \mapsto \psi \overset{j}{*} \phi$ maps $S(\mathbb{R}^n)$ continuously into itself.

Proof: We sketch the main steps of this proof. First, since we can differentiate under the integral sign, the function $\psi \overset{j}{*} \phi$ is infinitely differentiable for all $\phi, \psi \in S(\mathbb{R}^n)$. Furthermore, by means of a generalized product rule one can show that for every multi-index α , the derivative $\partial^\alpha (\psi \overset{j}{*} \phi)$ is a linear combination of partial convolutions of derivatives of ϕ and ψ . Combining this with the fact that $\mathbf{r}^\beta (\chi \overset{j}{*} \eta)$ is a bounded function for all multi-indices β and Schwartz functions χ, η , we find that $\mathbf{r}^\beta \partial^\alpha (\psi \overset{j}{*} \phi)$ is bounded too. In fact, it has an upper bound of the form $C p_{\alpha', \beta'}(\phi)$, where $C \geq 0$ depends on ψ . This finishes the proof. \square

Partial convolution is not only continuous, but also satisfies an identity analogous to [Equation 7.4](#), namely

$$\int_{\mathbb{R}^n} (\eta \overset{j}{*} \phi)(\mathbf{r}) \psi(\mathbf{r}) d\mathbf{r} = \int_{\mathbb{R}^n} \phi(\mathbf{r}) (M_j \eta \overset{j}{*} \psi)(\mathbf{r}) d\mathbf{r}$$

for all $\phi, \psi, \eta \in S(\mathbb{R}^n)$, where $M_j \phi(\mathbf{r}) = \phi(r_1, \dots, r_{j-1}, -r_j, r_{j+1}, \dots, r_n)$. Thus we can extend it to a continuous operation on $S'(\mathbb{R}^3)$ in the following way, recall [Remark 7.11](#).

Definition 7.21 (Partial convolution of a Schwartz function with a tempered distribution) The partial convolution of $\psi \in S(\mathbb{R}^n)$ with $v \in S'(\mathbb{R}^n)$ is defined by

$$(\psi \overset{j}{*} v)[\phi] := v[M_j \psi \overset{j}{*} \phi]$$

for all $\phi \in S(\mathbb{R}^n)$.

Finally, we have all prerequisites for formulating a one-dimensional convolution theorem for tempered distributions on \mathbb{R}^n .

Theorem 7.22 (Partial Convolution Theorem on $S'(\mathbb{R}^n)$) For all $\phi \in S(\mathbb{R}^n)$ and $v \in S'(\mathbb{R}^n)$, we have

$$\mathcal{F}_j(\phi \overset{j}{*} v) = (2\pi)^{\frac{1}{2}} \mathcal{F}_j \phi \mathcal{F}_j v, \quad \text{and} \quad \mathcal{F}_j \phi \overset{j}{*} \mathcal{F}_j v = (2\pi)^{\frac{1}{2}} \mathcal{F}_j(\phi v) \quad (7.9)$$

The same identities hold for \mathcal{F}_j^{-1} instead of \mathcal{F}_j .

Proof: First we observe that a corresponding one-dimensional convolution theorem for Schwartz functions, that is,

$$\mathcal{F}_j(\phi \overset{j}{*} \psi) = (2\pi)^{\frac{1}{2}} \mathcal{F}_j \phi \mathcal{F}_j \psi \quad \text{and} \quad \mathcal{F}_j \phi \overset{j}{*} \mathcal{F}_j \psi = (2\pi)^{\frac{1}{2}} \mathcal{F}_j(\phi \psi) \quad (7.10)$$

for all $\phi, \psi \in S(\mathbb{R}^n)$ holds true. Indeed, letting the coordinates r_i for $i \neq j$ be fixed, Equation 7.10 is nothing but a standard convolution theorem for the one-dimensional Schwartz functions $r_j \mapsto \phi(\mathbf{r})$ and $r_j \mapsto \psi(\mathbf{r})$.

Next, it follows directly from Definition 7.14 and Definition 7.21 that

$$\mathcal{F}_j(\phi \overset{j}{*} v)[\psi] = \phi \overset{j}{*} v[\mathcal{F}_j \psi] = v[M_j \phi \overset{j}{*} \mathcal{F}_j \psi].$$

The second identity in Equation 7.10 implies that

$$M_j \phi \overset{j}{*} \mathcal{F}_j \psi = (2\pi)^{\frac{1}{2}} \mathcal{F}_j \left((\mathcal{F}_j^{-1} M_j \phi) \psi \right) = (2\pi)^{\frac{1}{2}} \mathcal{F}_j ((\mathcal{F}_j \phi) \psi),$$

where we have also exploited the fact that $\mathcal{F}_j = \mathcal{F}_j^{-1} M_j$. Combining the previous two equalities gives

$$\mathcal{F}_j(\phi \overset{j}{*} v)[\psi] = (2\pi)^{\frac{1}{2}} v[\mathcal{F}_j ((\mathcal{F}_j \phi) \psi)] = (2\pi)^{\frac{1}{2}} \mathcal{F}_j v[(\mathcal{F}_j \phi) \psi] = (2\pi)^{\frac{1}{2}} (\mathcal{F}_j \phi) \mathcal{F}_j v[\psi].$$

In the last equality we have used the fact that multiplication of a tempered distribution with a Schwartz function is defined by $\phi v[\psi] = v[\phi \psi]$. This finishes the first part of Equation 7.9. The second part follows analogously, as do the corresponding formulas for the inverse \mathcal{F}_j^{-1} . \square

7.3. Proof of Theorem 3.1. In order to prove Theorem 3.1, we have to characterize the partial Fourier transform $\mathcal{F}_{1,2}G$, where the subscripts indicate that the transform is taken with respect to r_1 and r_2 and

$$G(\mathbf{r}) := \frac{e^{ik_0 \|\mathbf{r}\|}}{4\pi \|\mathbf{r}\|} \quad (7.11)$$

is the Green's function of the Helmholtz operator $-(\Delta + k_0^2)$ which satisfies the Sommerfeld radiation condition, see [8, Chap. 2]. Since $G(\cdot, \cdot, r_3)$ is not in $L^1(\mathbb{R}^2)$ for any $r_3 \in \mathbb{R}$, we cannot compute this transform $\mathcal{F}_{1,2}G$ as an ordinary Fourier integral. Instead, in Lemma 7.23 we calculate $\mathcal{F}_{1,2}G$ in the distributional sense. Mathematical details about distributions, (partial) Fourier transforms and convolutions can be found in Section 7.1 and Section 7.2.

We define

$$G_\epsilon(\mathbf{r}) := e^{-\epsilon \|\mathbf{r}\|} G(\mathbf{r}), \quad \epsilon > 0,$$

and note that $G_\epsilon \rightarrow G$ in $S'(\mathbb{R}^3)$ for $\epsilon \rightarrow 0$. We will also use the abbreviation

$$\kappa_\epsilon := \sqrt{(k_0 + i\epsilon)^2 - k_1^2 - k_2^2} \quad (7.12)$$

to denote the principal square root of $(k_0 + i\epsilon)^2 - k_1^2 - k_2^2$, that is, the root with positive imaginary part.

Lemma 7.23 *The partial Fourier transform $\mathcal{F}_{1,2}G \in S'(\mathbb{R}^3)$ is given by*

$$\mathcal{F}_{1,2}G[\phi] = \lim_{\epsilon \rightarrow 0} \mathcal{F}_{1,2}G_\epsilon[\phi] = \lim_{\epsilon \rightarrow 0} \int_{\mathbb{R}^3} \frac{ie^{i\kappa_\epsilon|r_3|}}{4\pi\kappa_\epsilon} \phi(k_1, k_2, r_3) d(k_1, k_2, r_3)$$

for all Schwartz functions $\phi \in S(\mathbb{R}^3)$.

Proof: Since $\mathcal{F}_{1,2}$ is continuous on $S'(\mathbb{R}^3)$, recall [Proposition 7.17](#), we also have $\mathcal{F}_{1,2}G_\epsilon \rightarrow \mathcal{F}_{1,2}G$ in $S'(\mathbb{R}^3)$. It remains to calculate $\mathcal{F}_{1,2}G_\epsilon$. We do so in two steps, according to [Equation 7.8](#).

First, exploiting the fact that G_ϵ is a radial function, see [\[38, Rem. 4.32\]](#), we obtain for the 3D Fourier transform

$$\mathcal{F}G_\epsilon(\mathbf{k}) = \|\mathbf{k}\|^{-1} (2\pi)^{-\frac{3}{2}} \int_0^\infty e^{s(-\epsilon + ik_0)} \sin(s\|\mathbf{k}\|) ds,$$

for all $\mathbf{k} \in \mathbb{R}^3$. The integral on the right-hand side can be calculated via integration by parts as

$$\mathcal{F}G_\epsilon(\mathbf{k}) = \frac{(2\pi)^{-\frac{3}{2}}}{\|\mathbf{k}\|^2 - (k_0 + i\epsilon)^2} = \frac{(2\pi)^{-\frac{3}{2}}}{k_3^2 - \kappa_\epsilon^2}.$$

Second, for $a \in \mathbb{C}$ with $\operatorname{Re} a > 0$, formula 17.23.14 in [\[19\]](#) states that

$$\int_{\mathbb{R}} \frac{e^{ik_3r_3}}{k_3^2 + a^2} dk_3 = \pi \frac{e^{-a|r_3|}}{a}.$$

With respect to the above integral, we use $a := -i\kappa_\epsilon$, which fulfills $\operatorname{Re} a > 0$ since $\operatorname{Im} \kappa_\epsilon > 0$. Then we obtain

$$\mathcal{F}_{1,2}G_\epsilon = \mathcal{F}_3^{-1} \mathcal{F}G_\epsilon = (2\pi)^{-2} \int_{\mathbb{R}} \frac{e^{ik_3r_3}}{k_3^2 - \kappa_\epsilon^2} dk_3 = -\frac{1}{4\pi} \frac{e^{i\kappa_\epsilon|r_3|}}{i\kappa_\epsilon}. \quad (7.13) \quad \square$$

Proof of Theorem 3.1: Let $g \in L^p(\mathbb{R}^3)$, $p > 1$, with $\operatorname{supp}(g) \subset \mathcal{B}_r$. Then, by the embedding in [Equation 7.1](#) and density of $\mathcal{D}(\mathbb{R}^3)$ in $L^p(\mathbb{R}^3)$, $p \in [1, \infty)$, we can find a sequence of functions $g_n \in \mathcal{D}(\mathbb{R}^3)$ with $\operatorname{supp} g_n \subset \mathcal{B}_r$, such that $g_n \rightarrow g$ in $L^q(\mathbb{R}^3)$, for $q \in [1, p]$ if $p \in (1, \infty)$ and for $q \in [1, \infty)$ otherwise, as $n \rightarrow \infty$. For each g_n , consider

$$(\Delta + k_0^2)u_n = -g_n$$

with the Sommerfeld radiation condition. The unique solution u_n is given by the convolution $u_n = g_n * G$, see [\[8, Chap. 2\]](#). From [Equation 7.8](#) and the convolution theorems [7.13](#) and [7.22](#), for the 3D Fourier transform \mathcal{F} and the partial Fourier transform \mathcal{F}_3 , it follows that

$$\begin{aligned} \mathcal{F}_{1,2}u_n &= \mathcal{F}_3^{-1} \mathcal{F}(g_n * G) = (2\pi)^{\frac{3}{2}} \mathcal{F}_3^{-1}(\mathcal{F}g_n \mathcal{F}G) = 2\pi (\mathcal{F}_3^{-1} \mathcal{F}g_n) \overset{3}{*} (\mathcal{F}_3^{-1} \mathcal{F}G) \\ &= 2\pi (\mathcal{F}_{1,2}g_n) \overset{3}{*} (\mathcal{F}_{1,2}G), \end{aligned} \quad (7.14)$$

where $\overset{3}{*}$ denotes the partial convolution with respect to the third coordinate. Now, for every $\phi \in S(\mathbb{R}^3)$, it follows by continuity of partial convolutions on $S'(\mathbb{R}^3)$ that

$$\begin{aligned} \mathcal{F}_{1,2}u_n[\phi] &= 2\pi \left(\mathcal{F}_{1,2}g_n \overset{3}{*} \mathcal{F}_{1,2}G \right) [\phi] = 2\pi \lim_{\epsilon \rightarrow 0} \left(\mathcal{F}_{1,2}g_n \overset{3}{*} \mathcal{F}_{1,2}G_\epsilon \right) [\phi] \\ &= 2\pi \lim_{\epsilon \rightarrow 0} \int_{\mathbb{R}^3} \mathcal{F}_{1,2}G_\epsilon [M_3 \mathcal{F}_{1,2}g_n \overset{3}{*} \phi] d(k_1, k_2, r_3), \end{aligned}$$

and by Fubini's theorem and [Equation 7.13](#) further

$$\mathcal{F}_{1,2}u_n[\phi] = \frac{i}{2} \lim_{\epsilon \rightarrow 0} \int_{\mathbb{R}^3} \frac{\phi}{\kappa_\epsilon} \int_{\mathbb{R}} e^{i\kappa_\epsilon|r_3-x|} \mathcal{F}_{1,2}g_n(k_1, k_2, x) dx d(k_1, k_2, r_3).$$

In order to change integration and limit, we will apply Lebesgue's dominated convergence theorem twice. First, noting that $\mathcal{F}_{1,2}g_n(k_1, k_2, \cdot) \in L^1(\mathbb{R})$ we conclude by Lebesgue's theorem that

$$\lim_{\epsilon \rightarrow 0} \int_{\mathbb{R}} e^{i\kappa_\epsilon|r_3-x|} \mathcal{F}_{1,2}g_n(k_1, k_2, x) dx = \int_{\mathbb{R}} e^{i\kappa|r_3-x|} \mathcal{F}_{1,2}g_n(k_1, k_2, x) dx,$$

for all $(k_1, k_2, r_3) \in \mathbb{R}^3$. It is then immediate that

$$\lim_{\epsilon \rightarrow 0} \frac{\phi(k_1, k_2, r_3)}{\kappa_\epsilon(k_1, k_2)} \int_{\mathbb{R}} e^{i\kappa_\epsilon|r_3-x|} \mathcal{F}_{1,2}g_n(k_1, k_2, x) dx = \frac{\phi(k_1, k_2, r_3)}{\kappa(k_1, k_2)} \int_{\mathbb{R}} e^{i\kappa|r_3-x|} \mathcal{F}_{1,2}g_n(k_1, k_2, x) dx \quad (7.15)$$

for $k_1^2 + k_2^2 \neq k_0^2$. In the following, we suppress the arguments of ϕ and κ for the sake of simplicity. The function $(k_1, k_2) \mapsto |\kappa|^{-1} = |k_0^2 - k_1^2 - k_2^2|^{-1/2}$ is locally integrable, since we have for $c > k_0$ in cylindrical coordinates that

$$\int_{B_c} |k_0^2 - k_1^2 - k_2^2|^{-1/2} d(k_1, k_2) = 2\pi \int_0^c \rho |k_0^2 - \rho^2|^{-1/2} d\rho = 2\pi(k_0 + \sqrt{c^2 - k_0^2}).$$

Using this integrability and $|\kappa| \leq |\kappa_\epsilon|$, it follows that

$$\left| \frac{\phi}{\kappa_\epsilon} \int_{\mathbb{R}} e^{i\kappa_\epsilon|r_3-x|} \mathcal{F}_{1,2}g_n(k_1, k_2, x) dx \right| \leq \frac{|\phi|}{|\kappa|} \int_{\mathbb{R}} |\mathcal{F}_{1,2}g_n(k_1, k_2, x)| dx \leq \frac{|\phi|}{2\pi|\kappa|} \|g_n\|_{L^1} \in L^1(\mathbb{R}^3). \quad (7.16)$$

Taking into account [Equation 7.15](#) and [Equation 7.16](#) and applying Lebesgue's dominated convergence theorem again, then gives

$$\mathcal{F}_{1,2}u_n[\phi] = \frac{i}{2} \int_{\mathbb{R}^3} \frac{\phi}{\kappa} \int_{\mathbb{R}} e^{i\kappa|r_3-x|} \mathcal{F}_{1,2}g_n(k_1, k_2, x) dx d(k_1, k_2, r_3).$$

Next, we can express

$$\begin{aligned} & \int_{\mathbb{R}} e^{i\kappa|r_3-x|} \mathcal{F}_{1,2}g_n(k_1, k_2, x) dx \\ &= e^{i\kappa r_3} \int_{-\infty}^{r_3} e^{-i\kappa x} \mathcal{F}_{1,2}g_n(k_1, k_2, x) dx + e^{-i\kappa r_3} \int_{r_3}^{+\infty} e^{i\kappa x} \mathcal{F}_{1,2}g_n(k_1, k_2, x) dx \\ &= e^{i\kappa r_3} \int_{\mathbb{R}} (1 - H_{r_3}(k_1, k_2, x)) e^{-i\kappa x} \mathcal{F}_{1,2}g_n(k_1, k_2, x) dx \\ & \quad + e^{-i\kappa r_3} \int_{\mathbb{R}} H_{r_3}(k_1, k_2, x) e^{i\kappa x} \mathcal{F}_{1,2}g_n(k_1, k_2, x) dx \\ &= e^{i\kappa r_3} \int_{\mathbb{R}} e^{-i\kappa x} \mathcal{F}_{1,2}((1 - H_{r_3})g_n)(k_1, k_2, x) dx + e^{-i\kappa r_3} \int_{\mathbb{R}} e^{i\kappa x} \mathcal{F}_{1,2}(H_{r_3}g_n)(k_1, k_2, x) dx \\ &= \sqrt{2\pi} (e^{i\kappa r_3} \mathcal{F}((1 - H_{r_3})g_n)(k_1, k_2, \kappa) + e^{-i\kappa r_3} \mathcal{F}(H_{r_3}g_n)(k_1, k_2, -\kappa)), \end{aligned} \quad (7.17)$$

where we recall that for $k_1, k_2 \in \mathbb{R}$ such that $k_1^2 + k_2^2 > k_0^2$, the analytic continuations of $\mathcal{F}((1 - H_{r_3})g_n)$ and $\mathcal{F}(H_{r_3}g_n)$ to \mathbb{C}^3 have to be considered. Therefore, we have

$$\begin{aligned} & \mathcal{F}_{1,2}u_n[\phi] \\ &= \frac{i\sqrt{\pi}}{\sqrt{2}} \int_{\mathbb{R}^3} \frac{\phi}{\kappa} (e^{i\kappa r_3} \mathcal{F}((1 - H_{r_3})g_n)(k_1, k_2, \kappa) + e^{-i\kappa r_3} \mathcal{F}(H_{r_3}g_n)(k_1, k_2, -\kappa)) d(k_1, k_2, r_3). \end{aligned} \quad (7.18)$$

We consider $n \rightarrow \infty$ in [Equation 7.18](#) and start with the right-hand side. Taking into account $g_n \rightarrow g$ in $L^1(\mathbb{R}^3)$ and $\mathcal{F} : L^1(\mathbb{R}^3) \rightarrow C_0(\mathbb{R}^3)$, we obtain the pointwise limit

$$\begin{aligned} & \lim_{n \rightarrow \infty} \frac{\phi}{\kappa} \left(e^{i\kappa r_3} \mathcal{F}((1 - H_{r_3})g_n)(k_1, k_2, \kappa) + e^{-i\kappa r_3} \mathcal{F}(H_{r_3}g_n)(k_1, k_2, -\kappa) \right) \\ &= \frac{\phi}{\kappa} \left(e^{i\kappa r_3} \mathcal{F}((1 - H_{r_3})g)(k_1, k_2, \kappa) + e^{-i\kappa r_3} \mathcal{F}(H_{r_3}g)(k_1, k_2, -\kappa) \right) \end{aligned} \quad (7.19)$$

for $k_1^2 + k_2^2 \neq k_0^2$. Further, we have

$$\left| \frac{\phi}{\kappa} \left(e^{i\kappa r_3} \mathcal{F}((1 - H_{r_3})g_n)(k_1, k_2, \kappa) + e^{-i\kappa r_3} \mathcal{F}(H_{r_3}g_n)(k_1, k_2, -\kappa) \right) \right| \leq \frac{|\phi|}{(2\pi)^{3/2} |\kappa|} \|g_n\|_{L^1}$$

for $k_1^2 + k_2^2 \neq k_0^2$, which follows from [Equation 7.16](#) and [Equation 7.17](#). As $g_n \rightarrow g$ in $L^1(\mathbb{R}^3)$, we can then find a constant $C > 0$ and $N \in \mathbb{N}$ such that

$$\left| \frac{\phi}{\kappa} \left(e^{i\kappa r_3} \mathcal{F}((1 - H_{r_3})g_n)(k_1, k_2, \kappa) + e^{-i\kappa r_3} \mathcal{F}(H_{r_3}g_n)(k_1, k_2, -\kappa) \right) \right| \leq C \frac{|\phi|}{\kappa} \|g\|_{L^1} \in L^1(\mathbb{R}^3) \quad (7.20)$$

for every $n \geq N$ and almost every $(k_1, k_2, r_3) \in \mathbb{R}^3$. With [Equation 7.19](#) and [Equation 7.20](#) at our disposal, Lebesgue's dominated convergence theorem gives

$$\begin{aligned} & \lim_{n \rightarrow \infty} \int_{\mathbb{R}^3} \frac{\phi}{\kappa} \left(e^{i\kappa r_3} \mathcal{F}((1 - H_{r_3})g_n)(k_1, k_2, \kappa) + e^{-i\kappa r_3} \mathcal{F}(H_{r_3}g_n)(k_1, k_2, -\kappa) \right) d(k_1, k_2, r_3) \\ &= \int_{\mathbb{R}^3} \frac{\phi}{\kappa} \left(e^{i\kappa r_3} \mathcal{F}((1 - H_{r_3})g)(k_1, k_2, \kappa) + e^{-i\kappa r_3} \mathcal{F}(H_{r_3}g)(k_1, k_2, -\kappa) \right) d(k_1, k_2, r_3). \end{aligned} \quad (7.21)$$

Next, we consider the convergence of the left-hand side in [Equation 7.18](#). From [\[21, Thm. 6, Rem. 1\]](#), it follows that the unique solution u of [Equation 3.2](#) for $g \in L^{q_1}(\mathbb{R}^3)$ satisfying the Sommerfeld radiation condition, fulfills

$$\|u\|_{L^{q_2}} \leq C(k_0) \|g\|_{L^{q_1}} \quad (7.22)$$

if $q_1 < \frac{3}{2}$, $q_2 > 3$ and $\frac{1}{2} \leq \frac{1}{q_1} - \frac{1}{q_2} \leq \frac{2}{3}$. In particular, $q_2 = 3 + \varepsilon$ and $q_1 \in [9 + 3\varepsilon/(9 + 2\varepsilon), 6 + 2\varepsilon/(5 + \varepsilon)]$ fulfill the above requirements for $\varepsilon > 0$ small enough. Thus, for every $p > 1$, we can find $1 < q_1 < p$ by setting ε small enough. For $g \in L^p(\mathbb{R}^3)$, $p > 1$ supported in \mathcal{B}_r , we know by the embedding in [Equation 7.1](#) that $g \in L^{q_1}(\mathbb{R}^3)$, for $1 < q_1 < p$. Thus, [Equation 7.22](#) implies that $u_n \rightarrow u$ in $L^{q_2}(\mathbb{R}^3)$, since $g_n \rightarrow g$ in $L^{q_1}(\mathbb{R}^3)$. In particular, $u_n \rightarrow u$ in $S'(\mathbb{R}^3)$. Then the continuity of $\mathcal{F}_{1,2}$ on $S'(\mathbb{R}^3)$ gives

$$\mathcal{F}_{1,2}u[\phi] = \lim_{n \rightarrow \infty} \mathcal{F}_{1,2}u_n[\phi] \quad (7.23)$$

for all $\phi \in S(\mathbb{R}^3)$ and by [Equation 7.21](#) finally

$$\begin{aligned} & \mathcal{F}_{1,2}u[\phi] \\ &= \frac{i\sqrt{\pi}}{\sqrt{2}} \int_{\mathbb{R}^3} \underbrace{\phi \frac{1}{\kappa} \left(e^{i\kappa r_3} \mathcal{F}((1 - H_{r_3})g)(k_1, k_2, \kappa) + e^{-i\kappa r_3} \mathcal{F}(H_{r_3}g)(k_1, k_2, -\kappa) \right)}_{\in L^1_{\text{loc}}(\mathbb{R}^3)} d(k_1, k_2, r_3). \end{aligned}$$

for all $\phi \in \mathcal{D}(\mathbb{R}^3)$. Then the assertion follows by applying the du Bois–Reymond lemma, see [\[20, Lem. 3.2\]](#). \square

7.4. Proof of Lemma 4.2. In this subsection we compute the determinant of the Jacobian $|\nabla T_{\pm}(k_1, k_2, t)|$.

Proof: By definition we have

$$|\nabla T_{\pm}(k_1, k_2, t)| = \left| \det \left(\frac{\partial}{\partial k_1} R_{\mathbf{n}(t), \alpha(t)} \mathbf{h}, \frac{\partial}{\partial k_2} R_{\mathbf{n}(t), \alpha(t)} \mathbf{h}, \frac{\partial}{\partial t} R_{\mathbf{n}(t), \alpha(t)} \mathbf{h} \right) \right|, \quad (7.24)$$

where the first and second columns are given by

$$\begin{aligned} \frac{\partial}{\partial k_1} R_{\mathbf{n}, \alpha} \mathbf{h} &= R_{\mathbf{n}, \alpha} \frac{\partial}{\partial k_1} \mathbf{h} = R_{\mathbf{n}, \alpha} \begin{pmatrix} 1 \\ 0 \\ \mp k_1 / \kappa \end{pmatrix}, \\ \frac{\partial}{\partial k_2} R_{\mathbf{n}, \alpha} \mathbf{h} &= R_{\mathbf{n}, \alpha} \frac{\partial}{\partial k_2} \mathbf{h} = R_{\mathbf{n}, \alpha} \begin{pmatrix} 0 \\ 1 \\ \mp k_2 / \kappa \end{pmatrix}. \end{aligned}$$

Multiplying the argument of the determinant in Equation 7.24 with the orthogonal matrix $R_{\mathbf{n}(t), -\alpha(t)} = R_{\mathbf{n}(t), \alpha(t)}^{-1}$ does not change the determinant. Hence we get

$$\begin{aligned} |\nabla T_{\pm}(k_1, k_2, t)| &= \left| \det \left(\frac{\partial}{\partial k_1} \mathbf{h}, \frac{\partial}{\partial k_2} \mathbf{h}, R_{\mathbf{n}(t), -\alpha(t)} \frac{\partial}{\partial t} R_{\mathbf{n}(t), \alpha(t)} \mathbf{h} \right) \right| \\ &= \left| \det \begin{pmatrix} 1 & 0 & v_1 \\ 0 & 1 & v_2 \\ \mp \frac{k_1}{\kappa} & \mp \frac{k_2}{\kappa} & v_3 \end{pmatrix} \right| \\ &= \left| \frac{k_1}{\kappa} v_1 + \frac{k_2}{\kappa} v_2 \pm v_3 \right|, \end{aligned} \quad (7.25)$$

where

$$\mathbf{v} = (v_1, v_2, v_3)^{\top} := R_{\mathbf{n}(t), -\alpha(t)} \frac{\partial}{\partial t} R_{\mathbf{n}(t), \alpha(t)} \mathbf{h}.$$

In the rest of this proof we calculate \mathbf{v} . To shorten our notation, we suppress the dependency on t and set $c := \cos(\alpha(t))$ and $s := \sin(\alpha(t))$. We set

$$\begin{aligned} \mathbf{z} := \frac{\partial}{\partial t} R_{\mathbf{n}(t), \alpha(t)} \mathbf{h} &= (1 - c) \left((\mathbf{n}' \cdot \mathbf{h}) \mathbf{n} + (\mathbf{n} \cdot \mathbf{h}) \mathbf{n}' \right) + \alpha' s \left((\mathbf{n} \cdot \mathbf{h}) \mathbf{n} - \mathbf{h} \right) \\ &\quad - \alpha' c \left(\mathbf{n} \times \mathbf{h} \right) - s \left(\mathbf{n}' \times \mathbf{h} \right), \end{aligned}$$

where the second equality is a consequence of Rodrigues' rotation formula

$$R_{\mathbf{n}, \alpha} \mathbf{y} = (1 - \cos(\alpha)) (\mathbf{n} \cdot \mathbf{y}) \mathbf{n} + \cos(\alpha) \mathbf{y} - \sin(\alpha) (\mathbf{n} \times \mathbf{y}). \quad (7.26)$$

Then we have

$$\mathbf{v} = R_{\mathbf{n}(t), -\alpha(t)} \mathbf{z} = (1 - c) (\mathbf{n} \cdot \mathbf{z}) \mathbf{n} + c \mathbf{z} + s (\mathbf{n} \times \mathbf{z}).$$

Since $\mathbf{n} \cdot \mathbf{n} = 1$ and consequently $\mathbf{n} \cdot \mathbf{n}' = 0$, we obtain

$$\begin{aligned} \mathbf{v} &= R_{\mathbf{n}(t), -\alpha(t)} \mathbf{z} = (1 - c) \mathbf{n} \left((1 - c) (\mathbf{n}' \cdot \mathbf{h}) - s \mathbf{n} \cdot (\mathbf{n}' \times \mathbf{h}) \right) \\ &\quad + c \left((1 - c) \left((\mathbf{n}' \cdot \mathbf{h}) \mathbf{n} + (\mathbf{n} \cdot \mathbf{h}) \mathbf{n}' \right) + \alpha' s \left((\mathbf{n} \cdot \mathbf{h}) \mathbf{n} - \mathbf{h} \right) - \alpha' c \left(\mathbf{n} \times \mathbf{h} \right) - s \left(\mathbf{n}' \times \mathbf{h} \right) \right) \\ &\quad + s \left((1 - c) (\mathbf{n} \cdot \mathbf{h}) (\mathbf{n} \times \mathbf{n}') - \alpha' s (\mathbf{n} \times \mathbf{h}) - \alpha' c (\mathbf{n} \times (\mathbf{n} \times \mathbf{h})) - s (\mathbf{n} \times (\mathbf{n}' \times \mathbf{h})) \right). \end{aligned}$$

Expanding the vector triple products in the last line using the Grassmann identity, we see that

$$\begin{aligned} \mathbf{v} &= (1 - c) \mathbf{n} \left((1 - c) (\mathbf{n}' \cdot \mathbf{h}) - s \mathbf{n} \cdot (\mathbf{n}' \times \mathbf{h}) \right) + c(1 - c) \left((\mathbf{n}' \cdot \mathbf{h}) \mathbf{n} + (\mathbf{n} \cdot \mathbf{h}) \mathbf{n}' \right) \\ &\quad + \alpha' c s \left((\mathbf{n} \cdot \mathbf{h}) \mathbf{n} - \mathbf{h} \right) - \alpha' c^2 (\mathbf{n} \times \mathbf{h}) - c s (\mathbf{n}' \times \mathbf{h}) + s(1 - c) (\mathbf{n} \cdot \mathbf{h}) (\mathbf{n} \times \mathbf{n}') \\ &\quad - \alpha' s^2 (\mathbf{n} \times \mathbf{h}) - \alpha' s c (\mathbf{n} (\mathbf{n} \cdot \mathbf{h}) - \mathbf{h}) - s^2 (\mathbf{n}' (\mathbf{n} \cdot \mathbf{h})). \end{aligned}$$

Sorting the terms, we obtain

$$\begin{aligned} \mathbf{v} &= \mathbf{n} \left((1-c)^2 (\mathbf{n}' \cdot \mathbf{h}) - s(1-c) \mathbf{n} \cdot (\mathbf{n}' \times \mathbf{h}) + c(1-c) (\mathbf{n}' \cdot \mathbf{h}) \right) \\ &\quad + \mathbf{n}' \left(c(1-c) (\mathbf{n} \cdot \mathbf{h}) - s^2 (\mathbf{n} \cdot \mathbf{h}) - \alpha' (\mathbf{n} \times \mathbf{h}) - sc (\mathbf{n}' \times \mathbf{h}) + s(1-c) (\mathbf{n} \cdot \mathbf{h}) (\mathbf{n} \times \mathbf{n}') \right) \\ &= \mathbf{n} \left((1-c) (\mathbf{n}' \cdot \mathbf{h}) - s(1-c) \mathbf{n} \cdot (\mathbf{n}' \times \mathbf{h}) \right) - \mathbf{n}' (1-c) (\mathbf{n} \cdot \mathbf{h}) \\ &\quad - \alpha' (\mathbf{n} \times \mathbf{h}) - sc (\mathbf{n}' \times \mathbf{h}) + s(1-c) (\mathbf{n} \cdot \mathbf{h}) (\mathbf{n} \times \mathbf{n}'). \end{aligned}$$

If $\mathbf{n}' = \mathbf{0}$, then $\mathbf{v} = -\alpha' (\mathbf{n} \times \mathbf{h})$. Otherwise, the vectors \mathbf{n} , \mathbf{n}' and $\mathbf{n} \times \mathbf{n}'$ are orthogonal and Lagrange's identity yields

$$\begin{aligned} \mathbf{n}' \times \mathbf{h} &= \mathbf{n} (\mathbf{n} \cdot (\mathbf{n}' \times \mathbf{h})) + \frac{1}{\|\mathbf{n} \times \mathbf{n}'\|^2} (\mathbf{n} \times \mathbf{n}') ((\mathbf{n} \times \mathbf{n}') \cdot (\mathbf{n}' \times \mathbf{h})) \\ &= \mathbf{n} (\mathbf{n} \cdot (\mathbf{n}' \times \mathbf{h})) - (\mathbf{n} \times \mathbf{n}') (\mathbf{n} \cdot \mathbf{h}). \end{aligned}$$

Hence, we obtain

$$\begin{aligned} \mathbf{v} &= \mathbf{n} \left((1-c) (\mathbf{n}' \cdot \mathbf{h}) - s(1-c) \mathbf{n} \cdot (\mathbf{n}' \times \mathbf{h}) \right) \\ &\quad - \mathbf{n}' (1-c) (\mathbf{n} \cdot \mathbf{h}) - \alpha' (\mathbf{n} \times \mathbf{h}) - sc (\mathbf{n} (\mathbf{n} \cdot (\mathbf{n}' \times \mathbf{h})) - (\mathbf{n} \times \mathbf{n}') (\mathbf{n} \cdot \mathbf{h})) \\ &\quad + s(1-c) (\mathbf{n} \cdot \mathbf{h}) (\mathbf{n} \times \mathbf{n}') \\ &= (1-c) (\mathbf{n} (\mathbf{n}' \cdot \mathbf{h}) - \mathbf{n}' (\mathbf{n} \cdot \mathbf{h})) - \mathbf{n} s (\mathbf{n} \cdot (\mathbf{n}' \times \mathbf{h})) - \alpha' (\mathbf{n} \times \mathbf{h}) + s (\mathbf{n} \cdot \mathbf{h}) (\mathbf{n} \times \mathbf{n}'). \end{aligned} \tag{7.27}$$

By [Equation 7.25](#), we have

$$|\nabla T_{\pm}(k_1, k_2, t)| = \left| \begin{pmatrix} v_1 \\ v_2 \\ v_3 \end{pmatrix} \cdot \begin{pmatrix} k_1/\kappa \\ k_2/\kappa \\ \pm 1 \end{pmatrix} \right| = \frac{1}{\kappa} \left| \begin{pmatrix} v_1 \\ v_2 \\ v_3 \end{pmatrix} \cdot \begin{pmatrix} k_1 \\ k_2 \\ \pm \kappa \end{pmatrix} \right| = \frac{1}{\kappa} \left| \mathbf{v} \cdot \left(\mathbf{h} + \begin{pmatrix} 0 \\ 0 \\ k_0 \end{pmatrix} \right) \right| = \frac{k_0}{\kappa} |v_3|,$$

where the last equality follows from $\mathbf{v} \cdot \mathbf{h} = 0$. Replacing v_3 by the third component of [Equation 7.27](#) yields

$$\begin{aligned} |\nabla T_{\pm}(k_1, k_2, t)| &= \frac{k_0}{\kappa} \left| ((1-c) (n_3 (\mathbf{n}' \cdot \mathbf{h}) - n'_3 (\mathbf{n} \cdot \mathbf{h})) - n_3 s \mathbf{n} \cdot (\mathbf{n}' \times \mathbf{h})) \right. \\ &\quad \left. - \alpha' (n_1 k_2 - n_2 k_1) + s (\mathbf{n} \cdot \mathbf{h}) (n_1 n'_2 - n_2 n'_1) \right|, \end{aligned}$$

which proves the first assertion. The Jacobian determinant is in $L^1(\mathcal{U})$, because $(k_1, k_2) \mapsto 1/\kappa(k_1, k_2)$ is locally integrable on \mathbb{R}^2 while the remaining expression is bounded on \mathcal{U} . \square

Acknowledgements. This work is supported by the Austrian Science Fund (FWF) within SFB F68 (“Tomography across the Scales”), Projects F68-06 and F68-07. G.S. acknowledges funding by the DFG under Germany’s Excellence Strategy – The Berlin Mathematics Research Center MATH+ (EXC-2046/1, Projektnummer: 390685689).

REFERENCES

- [1] S. R. Arridge. “Optical tomography in medical imaging”. In: *Inverse Problems* 15.2 (1999), R41–R93. ISSN: 0266-5611 (cited on page 1).
- [2] S. R. Arridge and J. C. Hebden. “Optical imaging in medicine: II. Modelling and reconstruction”. In: *Physics in Medicine & Biology* 42.5 (1997), pp. 841–853. ISSN: 0031-9155. DOI: [10.1088/0031-9155/42/5/008](https://doi.org/10.1088/0031-9155/42/5/008) (cited on page 1).

- [3] S. R. Arridge and J. Schotland. “Optical tomography: forward and inverse problems”. In: *Inverse Problems* 25 (2009), p. 123010. ISSN: 0266-5611 (cited on page 1).
- [4] G. Beylkin. “On the fast Fourier transform of functions with singularities”. In: *Appl. Comput. Harmon. Anal.* 2.4 (1995), pp. 363–381. DOI: [10.1006/acha.1995.1026](https://doi.org/10.1006/acha.1995.1026) (cited on page 16).
- [5] V. Bogachev. “Measure Theory”. Vol. 1. Springer Berlin Heidelberg, 2007 (cited on page 9).
- [6] W. Choi, C. Fang-Yen, S. Oh, N. Lue, K. Badizadegan, R. R. Dasari, and M. S. Feld. “Tomographic Phase Microscopy—Quantitative 3D Imaging of Living Cells”. In: *BIOforum Europe* 11.10 (2007), pp. 24–25. ISSN: 1611-597X (cited on page 2).
- [7] R. R. Coifman, Y. Shkolnisky, F. J. Sigworth, and A. Singer. “Reference Free Structure Determination through Eigenvectors of Center of Mass Operators”. In: *Applied and Computational Harmonic Analysis* 28.3 (2010), pp. 296–312. ISSN: 1063-5203. DOI: [10.1016/j.acha.2009.11.003](https://doi.org/10.1016/j.acha.2009.11.003) (cited on page 3).
- [8] D. Colton and R. Kress. “Inverse Acoustic and Electromagnetic Scattering Theory”. 3rd ed. Applied Mathematical Sciences 93. Berlin: Springer, 2013. ISBN: 978-1-4614-4941-6. DOI: [10.1007/978-1-4614-4942-3](https://doi.org/10.1007/978-1-4614-4942-3) (cited on pages 27, 28).
- [9] A. J. Devaney. “A filtered backpropagation algorithm for diffraction tomography”. In: *Ultrasonic Imaging* 4 (1982), pp. 336–350 (cited on pages 2, 3).
- [10] A. J. Devaney. “Geophysical Diffraction Tomography”. In: *IEEE Transactions on Geoscience and Remote Sensing* GE-22.1 (1984), pp. 3–13. DOI: [10.1109/tgrs.1984.350573](https://doi.org/10.1109/tgrs.1984.350573) (cited on pages 2, 3).
- [11] A. J. Devaney. “Inverse source and scattering problems in ultrasonics”. In: *IEEE Transactions on Sonics and Ultrasonics* 4 (1983), pp. 336–350 (cited on pages 2, 3).
- [12] A. J. Devaney. “Inverse-scattering theory within the Rytov approximation”. In: *Optics Letters* 6.8 (1981), p. 374. DOI: [10.1364/ol.6.000374](https://doi.org/10.1364/ol.6.000374) (cited on page 3).
- [13] K. Dholakia, B. W. Drinkwater, and M. Ritsch-Marte. “Comparing acoustic and optical forces for biomedical research”. In: *Nature Reviews Physics* 2.9 (2020), pp. 480–491 (cited on page 2).
- [14] A. Dutt and V. Rokhlin. “Fast Fourier transforms for nonequispaced data”. In: *SIAM J. Sci. Stat. Comput.* 14.6 (1993), pp. 1368–1393. DOI: [10.1137/0914081](https://doi.org/10.1137/0914081) (cited on page 16).
- [15] P. Elbau, M. Ritsch-Marte, O. Scherzer, and D. Schmutz. “Motion Reconstruction for Optical Tomography of Trapped Objects”. In: *Inverse Problems* 36.4 (2020), p. 044004. ISSN: 0266-5611 (cited on page 3).
- [16] H. W. Engl, M. Hanke, and A. Neubauer. “Regularization of inverse problems”. Vol. 375. Mathematics and Its Applications. Kluwer Academic Publishers, 1996. ISBN: 0-7923-4157-0 (cited on page 21).
- [17] J. R. Fienup. “Reconstruction of a complex-valued object from the modulus of its Fourier transform using a support constraint”. In: *JOSA A* 4.1 (1987), pp. 118–123 (cited on page 2).
- [18] A. B. Goncharov. “Methods of integral geometry and recovering a function with compact support from its projections in unknown directions”. In: *Acta Applicandae Mathematicae* 11.3 (1988), pp. 213–222. DOI: [10.1007/BF00140119](https://doi.org/10.1007/BF00140119) (cited on page 3).
- [19] I. S. Gradshteyn and I. M. Ryzhik. “Table of Integrals, Series, and Products”. Seventh. Academic Press New York, 2007 (cited on page 28).
- [20] G. Grubb. “Distributions and operators”. Vol. 252. Graduate Texts in Mathematics. Springer, New York, 2009 (cited on pages 6, 22, 24, 30).

- [21] S. Gutiérrez. “Non trivial L^q solutions to the Ginzburg-Landau equation”. In: *Math. Ann.* 328.1–2 (2004), pp. 1–25. DOI: [10.1007/s00208-003-0444-7](https://doi.org/10.1007/s00208-003-0444-7) (cited on page 30).
- [22] U. Hämarik and R. Palm. “On rules for stopping the conjugate gradient type methods in ill-posed problems”. In: *Math. Model. Anal.* 12 (1 2007), pp. 61–70. DOI: [10.3846/1392-6292.2007.12.61-70](https://doi.org/10.3846/1392-6292.2007.12.61-70) (cited on page 21).
- [23] P. C. Hansen. “Analysis of Discrete Ill-Posed Problems by Means of the L-Curve”. en. In: *SIAM Review* 34.4 (1992), pp. 561–580. ISSN: 0036-1445, 1095-7200. DOI: [10.1137/1034115](https://doi.org/10.1137/1034115) (cited on page 21).
- [24] P. C. Hansen. “Regularization Tools version 4.0 for Matlab 7.3”. en. In: *Numer. Algo.* 46.2 (2007), pp. 189–194. DOI: [10.1007/s11075-007-9136-9](https://doi.org/10.1007/s11075-007-9136-9) (cited on page 21).
- [25] M. van Heel. “Angular reconstitution: A posteriori assignment of projection directions for 3D reconstruction”. In: *Ultramicroscopy* 21.2 (1987), pp. 111–123. ISSN: 0304-3991. DOI: [10.1016/0304-3991\(87\)90078-7](https://doi.org/10.1016/0304-3991(87)90078-7) (cited on page 3).
- [26] L. Hörmander. “The Analysis of Linear Partial Differential Operators I”. 2nd ed. New York: Springer Verlag, 2003 (cited on page 22).
- [27] D. Jin, R. Zhou, Z. Yaqoob, and P. T. So. “Tomographic phase microscopy: principles and applications in bioimaging”. In: *JOSA B* 34.5 (2017), B64–B77 (cited on page 1).
- [28] A. C. Kak and M. Slaney. “Principles of Computerized Tomographic Imaging”. Vol. 33. Classics in Applied Mathematics. Philadelphia, PA: Society for Industrial and Applied Mathematics (SIAM), 2001 (cited on pages 4, 6).
- [29] J. Keiner, S. Kunis, and D. Potts. *NFFT 3.5, C subroutine library*. <https://www.tu-chemnitz.de/~potts/nfft> (cited on page 16).
- [30] W. Krauze. “Optical diffraction tomography with finite object support for the minimization of missing cone artifacts”. In: *Biomedical optics express* 11.4 (2020), pp. 1919–1926. DOI: [10.1364/BOE.386507](https://doi.org/10.1364/BOE.386507) (cited on page 2).
- [31] S. Kunis and D. Potts. “Stability results for scattered data interpolation by trigonometric polynomials”. In: *SIAM J. Sci. Comput.* 29 (2007), pp. 1403–1419. DOI: [10.1137/060665075](https://doi.org/10.1137/060665075) (cited on page 16).
- [32] J. Lim, K. Lee, K. H. Jin, S. Shin, S. Lee, Y. Park, and J. C. Ye. “Comparative study of iterative reconstruction algorithms for missing cone problems in optical diffraction tomography”. In: *Optics Express* 23.13 (2015), p. 16933. DOI: [10.1364/oe.23.016933](https://doi.org/10.1364/oe.23.016933) (cited on pages 2, 3).
- [33] A. K. Louis, T. Weber, and D. Theis. “Computing Reconstruction Kernels for Circular 3-D Cone Beam Tomography”. In: *IEEE Transactions on Medical Imaging* 27.7 (2008), pp. 880–886. ISSN: 0278-0062. DOI: [10.1109/tmi.2008.922188](https://doi.org/10.1109/tmi.2008.922188) (cited on page 9).
- [34] P. Mora. “Inversion = migration + tomography”. In: *Geophysics* 54.12 (1989), pp. 1575–1586. DOI: [10.1190/1.1442625](https://doi.org/10.1190/1.1442625) (cited on page 3).
- [35] P. Müller, M. Schürmann, and J. Guck. *The theory of diffraction tomography*. 2015. arXiv: [1507.00466](https://arxiv.org/abs/1507.00466) (cited on page 2).
- [36] F. Natterer. “Sonic Imaging”. In: *Handbook of Mathematical Methods in Imaging*. Ed. by O. Scherzer. 2nd ed. New York: Springer, 2015, pp. 1253–1278. ISBN: 978-1-4939-0789-2. DOI: [10.1007/978-3-642-27795-5_37-2](https://doi.org/10.1007/978-3-642-27795-5_37-2) (cited on page 3).
- [37] F. Natterer and F. Wübbeling. “Mathematical Methods in Image Reconstruction”. Monographs on Mathematical Modeling and Computation 5. Philadelphia, PA: SIAM, 2001 (cited on pages 3, 6).

- [38] G. Plonka, D. Potts, G. Steidl, and M. Tasche. “Numerical Fourier Analysis”. Applied and Numerical Harmonic Analysis. Birkhäuser, 2018. ISBN: 978-3-030-04305-6. DOI: [10.1007/978-3-030-04306-3](https://doi.org/10.1007/978-3-030-04306-3) (cited on pages 16, 17, 22, 28).
- [39] M. Reed and B. Simon. “Fourier Analysis, Self-Adjointness”. Vol. 2. Methods of Modern Mathematical Physics. Academic Press, 1975 (cited on page 22).
- [40] J. Sharpe, U. Ahlgren, P. Perry, B. Hill, A. Ross, J. Hecksher-Sørensen, R. Baldock, and D. Davidson. “Optical projection tomography as a tool for 3D microscopy and gene expression studies”. In: *Science* 296.5567 (2002), pp. 541–545 (cited on page 2).
- [41] A. Singer and Y. Shkolnisky. “Three-dimensional Structure Determination from Common Lines in Cryo-EM by Eigenvectors and Semidefinite Programming”. In: *SIAM Journal on Imaging Sciences* 4.2 (2011), pp. 543–572. ISSN: 1936-4954. DOI: [10.1137/090767777](https://doi.org/10.1137/090767777) (cited on page 3).
- [42] G. Steidl. “A Note on Fast Fourier Transforms for Nonequispaced Grids”. In: *Adv. Comput. Math.* 9.3 - 4 (1998), pp. 337–353. DOI: [10.1023/A:1018901926283](https://doi.org/10.1023/A:1018901926283) (cited on page 16).
- [43] Y. Sung and R. R. Dasari. “Deterministic regularization of three-dimensional optical diffraction tomography”. In: *Journal of the Optical Society of America A* 28.8 (2011), p. 1554. ISSN: 0764-583X. DOI: [10.1364/josaa.28.001554](https://doi.org/10.1364/josaa.28.001554) (cited on pages 2, 3).
- [44] Y. Sung, W. Choi, C. Fang-Yen, K. Badizadegan, R. R. Dasari, and M. S. Feld. “Optical diffraction tomography for high resolution live cell imaging”. In: *Optics express* 17.1 (2009), pp. 266–277 (cited on page 1).
- [45] L. Tian, X. Li, K. Ramchandran, and L. Waller. “Multiplexed coded illumination for Fourier Ptychography with an LED array microscope”. In: *Biomedical optics express* 5.7 (2014), pp. 2376–2389 (cited on page 2).
- [46] J. Virieux, A. Asnaashari, R. Brossier, L. Métivier, A. Ribodetti, and W. Zhou. “6. An introduction to full waveform inversion”. In: *Encyclopedia of Exploration Geophysics*. Society of Exploration Geophysicists, Jan. 2014, R1–1–R1–40. DOI: [10.1190/1.9781560803027.entry6](https://doi.org/10.1190/1.9781560803027.entry6) (cited on page 2).
- [47] L. Wang, A. Singer, and Z. Wen. “Orientation determination of cryo-EM images using least unsquared deviations”. In: *SIAM Journal on Imaging Sciences* 6.4 (2013), pp. 2450–2483. ISSN: 1936-4954. DOI: [10.1137/130916436](https://doi.org/10.1137/130916436) (cited on page 3).
- [48] Z. Wang, A. C. Bovik, H. R. Sheikh, and E. P. Simoncelli. “Image Quality Assessment: From Error Visibility to Structural Similarity”. In: *IEEE Trans. Image Process.* 13 (2004), pp. 600–612. DOI: [10.1109/TIP.2003.819861](https://doi.org/10.1109/TIP.2003.819861) (cited on page 17).
- [49] E. Wolf. “Three-dimensional structure determination of semi-transparent objects from holographic data”. In: *Optics Communications* 1 (1969), pp. 153–156 (cited on pages 4, 6).
- [50] R. Wu and M. Toksöz. “Diffraction tomography and multisource holography applied to seismic imaging”. In: *Geophysics* 52 (1987), pp. 11–25 (cited on page 3).